

Modification of fumarolic gases by the ice-covered edifice of Erebus volcano, Antarctica

T. Ilanko^{1,2*}, T.P. Fischer¹, P. Kyle³, A. Curtis^{3,4}, H. Lee^{1,5}, Y. Sano⁶

1. Department of Earth & Planetary Sciences, University of New Mexico, NM 87131, USA

2. Present address: Department of Geography, University of Sheffield, Sheffield S10 2TN, UK

3. Department of Earth & Environmental Science, N.M. Institute of Mining and Technology, Socorro, NM 87801, USA

4. Present address: Jet Propulsion Laboratory, Pasadena, CA91109, USA

5. Present address: School of Earth and Environmental Sciences, Seoul National University, 1 Gwanak-ro, Gwanak-gu, 08826 Seoul, South Korea

6. Institute of Atmosphere and Ocean Research, The University of Tokyo, Chiba, Japan

*Corresponding author: tehnuka@volcanofiles.com

Keywords

Fumarolic ice caves, volcanic degassing, carbon dioxide, Erebus volcano

Abstract

The chemistry of gases measured in ice caves and from warm geothermal ground at Erebus volcano, Antarctica, show that gas emissions are dominated by air, with varying amounts of added volcanic CO₂. This suggests widespread circulation of air through the volcanic edifice, as well as spatially or temporally varying contributions from magmatic degassing.

The resulting gases are further modified by two processes. The first is CO₂ dissolution in water, resulting in fractionation from magmatic $\delta^{13}\text{C-CO}_2$ values, which are estimated to be around -4‰, to heavier values, up to -1‰. Assuming all magmatic CO₂ is dissolved in neutral water as HCO₃⁻, this requires hydrothermal temperatures of over 120°C. However, other phases such as calcite may be present, likely implying even higher temperatures, while lower water pH values could result in similar isotope ratios at much lower temperatures, such as 60°C at pH of 5.3. A large proportion of magmatic CO₂ must be lost to this hydrothermal system or to mixing with air. The hydrothermal influence is localized to certain areas on the volcano, which may be associated with high velocity zones identified in previous studies by seismic tomography. Two sites with stronger magmatic signatures, by contrast, are above low velocity zones representing possible shallow magma storage.

The second modification is the removal of oxygen from both deeply-sourced and air-derived gases. This is likely due to prevailing conditions in the subsurface, as it is independent of the original source of the gases and of hydrothermal modifications, and thus may affect sites with magmatic, air-like, or hydrothermal signatures.

40 **1. Introduction**

41

42 **1.1 Hydrothermal systems at snow- or ice-covered volcanoes.**

43 Near surface heat and fumarolic gas emission on glaciated and snow-covered volcanoes, cause melting and
44 sublimation of the ice and snow and can result in the formation of fumarolic ice caves (FIC) (Curtis and Kyle,
45 2011, 2017). Globally, FIC have been described on only a few volcanoes, including Erebus and Mount
46 Melbourne in Antarctica (Lyon and Giggenbach, 1974), and Mount Rainier (Zimbelman et al., 2000), Mount
47 Baker, and Mount St Helens in the Cascades. However, it has been suggested that such systems may be more
48 common and widely distributed than the few known examples (Curtis and Kyle, 2017).

49

50 FIC conveniently reveal fumarolic or diffuse degassing sites that might be hard to observe on a volcano
51 without ice or snow cover. Understanding this degassing and potential hydrothermal circulation at glaciated
52 volcanoes also has implications for volcanic hazards. These include the likelihood of phreatic or
53 phreatomagmatic eruptions, or reduced slope stability due to hydrothermal alteration. Monitoring gas
54 emissions or ice cover at active volcanoes could be important in identifying changes to heat flow and
55 degassing that result from changes in shallow magmatic or hydrothermal systems. Moreover, glaciation and
56 deglaciation may act on a large scale as controls on volcanic activity and the climate, with the implication that
57 decreasing ice cover can cause increases in carbon dioxide emissions, and thus warming (Huybers and
58 Langmuir, 2009). Understanding degassing from glaciated volcanoes is important to both understanding past
59 changes in climate, such as the contribution of volcanic CO₂ to deglaciation, and the implications of
60 widespread ice loss in volcanic regions due to a warming climate. For example, over a hundred potential
61 subglacial volcanoes have been identified in West Antarctica (van Wyk de Vries et al., 2018) as well as
62 evidence for recent eruptions (Iverson et al., 2017), and possible ongoing magma movement (Lough et al.,
63 2013).

64

65 Due to the more limited ice cover in its summit area and the accessibility of Erebus, it is one of the few sites
66 where degassing of a glaciated volcano can be quantified. Erebus is unique among volcanoes currently hosting
67 ice caves in that it exhibits long-term persistent degassing through an open conduit, with many studies
68 focused on the dynamics and gas chemistry of its lava lake. However, also of interest in understanding its gas
69 flux, and more relevant to glaciated volcanoes lacking open summit vents, is the persistent flank degassing on
70 which our study focuses. The following section briefly describes the setting and volcanic activity of Erebus.

71

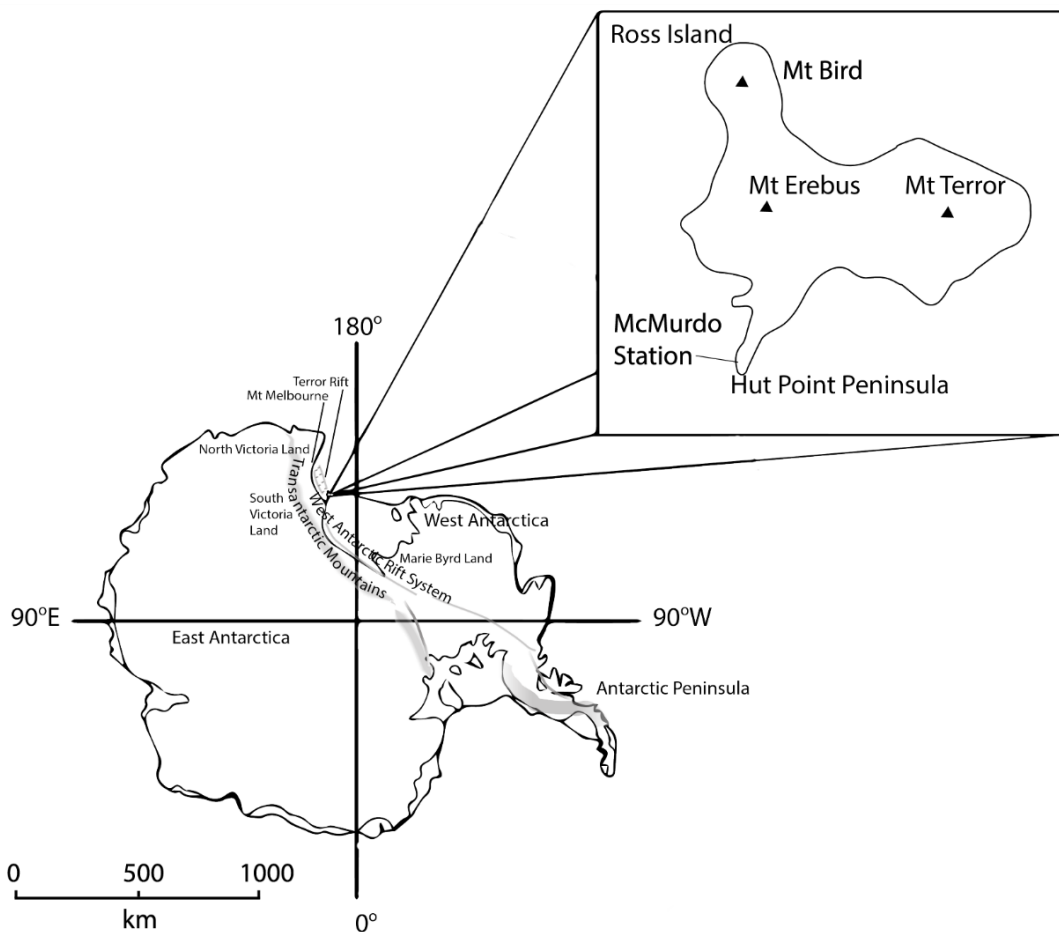
72

73 **1.2 Tectonic setting, Antarctic volcanism and Erebus volcano**

74 Erebus volcano (Fig. 1) is one of four volcanic centres on Ross Island at the southern end of the Terror Rift,
75 which has the youngest extension in the West Antarctic Rift System (WARS) (Hall et al., 2007; Henrys et al.,
76 2007). Although Erebus is presently the most active volcano in the WARS, degassing occurs at others (Mt
77 Berlin, Marie Byrd Land; Mts Rittmann and Melbourne, northern Victoria Land). The WARS covers the
78 margin between the Transantarctic Mountains and the crustal blocks, derived from the breakup of
79 Gondwana, that make up much of West Antarctica (Behrendt et al., 1991). Extension across the rift dates
80 from the Cretaceous and the end of subduction along the Gondwana margin, but there remains uncertainty
81 about whether the WARS is still active (Martin et al., 2014; Harry et al., 2018), and the relationship between
82 its tectonism and volcanic activity.

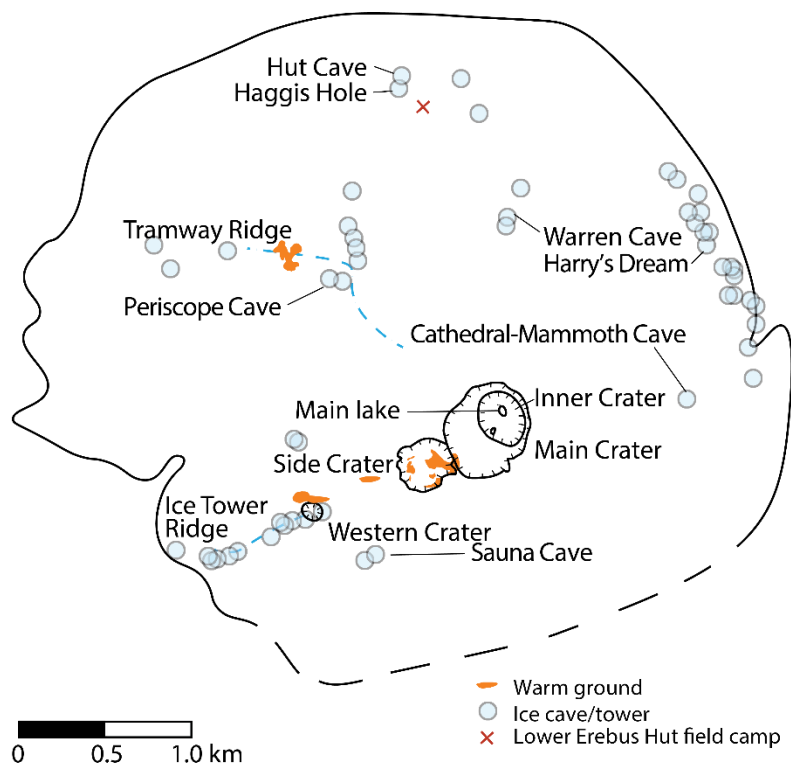
83

84 Late Cenozoic volcanism in the WARS has been attributed to mantle plumes or extension of the lower
 85 lithosphere causing decompression melting (Kyle et al., 1992; Behrendt, 1999; Rocchi et al., 2002). According
 86 to Rilling et al. (2009), the timing of rifting episodes and volcanism in the Terror Rift indicates decompression
 87 melting, though additional heat input or a modified mantle composition with a lower solidus are required to
 88 allow partial melting and volcanism. This is consistent with Panter et al. (2018) who attribute the
 89 geochemistry of lavas in the northwest Ross Sea to subcontinental lithospheric mantle (SCLM) with
 90 metasomatic veins formed by carbonate-rich partial melt from the asthenosphere, itself containing material
 91 subducted at the Gondwana margin. Ross Island, however, may be an exception. The HIMU (high $^{238}\text{U}/^{204}\text{Pb}$
 92 ratio mantle)-like composition of Ross Island lavas, and the presence of a seismic low velocity zone down to
 93 1200 km beneath Ross Island support the argument of Phillips et al. (2018) for upwelling from the
 94 asthenospheric mantle as the source of volcanism. A mantle plume (Kyle et al., 1992) could also account for
 95 the large volume magmatism, the radial arrangement of volcanic centres, and ongoing volcanism. No carbon
 96 isotope data are available for xenoliths on Ross Island but Correale et al. (2017) report carbon isotope ratios
 97 of -4.5‰ to -2.5‰, with -3.5‰ for samples containing high CO_2 , in SCLM xenoliths from northern Victoria
 98 Land. However, this may differ further south beneath Ross Island, given the evidence for an asthenospheric
 99 source and the suggestion by Phillips et al. (2018) that the metasomatized SCLM beneath Ross Island has
 100 been removed by mantle upwelling. Parmelee et al. (2015) report $^3\text{He}/^4\text{He}$ of 6.86 to 7.06 R_a for olivine from
 101 hyaloclastite at Hut Point Peninsula and suggested the range was representative of the mantle beneath Ross
 102 Island. This is consistent with both MORB and HIMU ranges (Anderson, 2000).



103
 104 **Figure 1.** Location of Ross Island and Erebus. McMURDO Station and Scott Base are located on the southern
 105 end of Hut Point Peninsula. WARS and Terror Rift after LeMasurier (1990, 2008).

106



107

108

109 **Figure 2.** Erebus caldera, with craters, major ice towers, and ice caves. Warm ground areas include areas
110 around Tramway Ridge (dashed line), Western Crater, and Side Crater. Data from Panter and Winter (2008),
111 Curtis and Kyle (2010), and field observations.

112

113 Erebus is perhaps best known for the long-lived phonolite lava lake in its summit cone. This cone rises from
114 a plateau on the upper flanks of the volcano, formed by two overlapping calderas at about 3400 m altitude,
115 which contains over 100 FIC. Descriptions of many of these FIC, reported over several expeditions, are
116 available through the Erebus caves database (Curtis and Kyle, 2010). At Erebus, the typical FIC is on the
117 boundary between rock and snowpack, and not within a glacier, although it should be noted that ice density is
118 closer to that of glacial ice than of firn (Curtis, 2015). A number of features of the caves are described by
119 Curtis (2015) including barometric pumping at entrances, hot vents in the rock floors as well as cold vents on
120 the surface through which outside air mixes in, and changes in the size and shape of caves between annual
121 field seasons. Known areas of upper flank degassing on Erebus (Fig. 2) include Ice Tower Ridge (ITR), a line
122 of small FIC extending from the southwest of the plateau through areas of warm ground on the flanks of the
123 summit cone, and terminating at Side Crater, itself containing a number of fumaroles and warm ground areas
124 (Panter and Winter, 2008). Other areas of interest include Tramway Ridge, which is an Antarctic Specially
125 Protected Area (ASPA) of warm ground to the northwest of the summit cone, and more extensive caves
126 located at various sites around the plateau including Hut Cave to the north, Warren Cave (NE), the
127 sometimes-connected Cathedral-Mammoth system (SE), and Sauna (S).

128

129 The active magmatic system at Erebus degasses through the lava lake(s) and nearby high temperature vents
130 with a composition rich in CO₂ relative to water and SO₂ (Oppenheimer and Kyle, 2008). Melt inclusions in
131 Ross Island basanites, which are considered representative of the parental melt for the Erebus phonolite,
contain up to 1.8% CO₂ (Rasmussen et al., 2017). Degassing at shallow depths is controlled by the solubility

132 of the various volatile species, but CO₂, which is relatively insoluble, may be sourced from the mantle
133 (Oppenheimer et al., 2011). Based on plume gas chemistry and melt inclusion volatile contents, deep
134 degassing is likely to be the biggest contributor to the lava lake gas plume, followed by degassing from the
135 lava lake, with limited input from intermediate regions (Iacovino, 2015). At shallow depths, seismic
136 tomography and interferometric studies by Zandomenighi et al. (2013) identify several low- and high-velocity
137 zones within hundreds of metres below the surface of the Erebus summit plateau. They suggest that these
138 correspond to hot magma bodies or high permeability zones, and cooled intrusions or buried lava and caldera
139 rim features, respectively. The complex shallow magmatic plumbing has been attributed to possible restriction
140 of fluid flow by the latter. Both low- and high-velocity zones may influence the location of degassing features
141 such as ice caves, and the nature of subsurface structures may be reflected in the gas measured at the surface.
142

143 Ice and snow cover are variable around the Erebus caldera. Only limited meteoric water recharge is possible
144 in the arid climate, but localized melting of ice and snow, associated with heat from FIC and warm ground
145 areas, is evident. Groundwater on the Antarctic continent includes brines beneath the permafrost in the Dry
146 Valleys (Mikucki et al., 2015), and groundwater in ice-covered regions, where it may have some association
147 with subglacial volcanism (Christoffersen et al., 2014). The nature of a hydrothermal system on Erebus has
148 not been directly addressed before, although the presence of any substantial amount of liquid water within the
149 volcanic edifice will have implications in assessing potential hazards.
150

151 Volcanic activity on Erebus has mostly been stable over the past century or more, dominated by passive
152 degassing and small Strombolian explosions from the lava lake and adjacent vents. However, two significant
153 phreatic eruptions occurred in October 1993, emitting debris described by Dibble et al. (1994) as
154 hydrothermally altered. Evidence of phreatomagmatic activity in the Side Crater was found by Panter &
155 Winter (2008) and attributed to melting from the surface or permafrost, or to shallow hydrothermal water.
156 Distal tephra layers indicate that frequent phreatoplinian eruptions have occurred in the past (Harpel et al.,
157 2008; Iverson et al., 2014) but these have been explained as a result of snow or ice accumulation within the
158 crater.
159

160 Here, we report gas compositions, carbon isotope and nitrogen isotope data, and CO₂ fluxes, which reflect
161 sources of degassing and modification by crustal or hydrothermal processes. Wardell et al. (2003) previously
162 investigated CO₂ fluxes and carbon isotope ratios at ice towers and warm ground areas, suggesting that the
163 measured carbon isotope ratios are due to mantle CO₂ sources, but without accounting for the range of
164 observed values. While a heterogeneous mantle source is one possibility, other processes such as dissolution
165 in water may also affect CO₂ degassing and carbon isotope composition. If magma bodies in the upper 400 m
166 of the volcanic edifice influence degassing, then we expect compositions of gases emitted above hot
167 intrusions as identified by Zandomenighi et al. (2013), where a magmatic signature is likely, to differ from
168 those emitted above cooled intrusions, where gases are potentially more deeply sourced but follow old
169 pathways, and are more susceptible to mixing with surface air or dissolution in meltwater.
170

171 **2. Methods**

172 **2.1 Gas sampling**

174 Samples were collected at vents or diffuse degassing sites, within caves and in warm ground areas. We
175 focused on sites that were known to have been entered in the past, due to the biological sensitivity of pristine

176 and little-visited caves. For gas composition, argon and nitrogen isotope analyses, samples were collected in
177 copper tubes and Giggenbach bottles (Giggenbach, 1975). Air samples were also collected inside and outside
178 caves, generally by opening a pre-evacuated vial or Giggenbach bottle. These provide samples for background
179 compositions. Samples for carbon dioxide isotope analyses were taken in 1L Tedlar bags for analysis at the
180 field camp with an infrared isotope ratio spectrometer.

181

182 **2.1.1 Soil probe and titanium tubes**

183 Samples were mostly collected using a 5V battery-powered pump, and a soil probe or titanium tube,
184 connected to sampling vessels by tygon tubing. The soil probe or tube was inserted as far as possible into soil
185 or gravel on the cave floors where temperatures were elevated, or into cracks in the rock where degassing was
186 observed. Typically, sampling vessels included a series of four 30 cm lengths of soft copper tubes with about
187 6 mm internal diameter, linked by short sections of tygon tubing. One end of this sample train was connected
188 to a 1 m soil probe, and the other to the intake of the pump. The pump outlet could be connected to a needle
189 that injected gas through the seal into a pre-evacuated 10 ml glass vial, with a second needle inserted into the
190 seal to maintain gas flow through the vial. In some instances, gas flow out from the vent was sufficient that
191 no pump was required. The highest airflow velocity from a vent was measured by an anemometer at over 6
192 m·s⁻¹ (Shooting Gallery, Ice Tower Ridge).

193

194 The pump and soil probe setup was left for several hours, and usually for one day, to flush out ambient air,
195 with the exception of high temperature sites at Sauna and Tramway (measured in 2016) where they were
196 collected after one hour. The battery and pump could operate for several days if required so that samples
197 were not lost in case a return to the site was delayed by bad weather. For collection, we removed the needles
198 from the vial, and cold-welded the ends of the copper tubes while they remained connected to the soil probe.

199

200 **2.1.2 Accumulation chamber**

201 To measure soil CO₂ fluxes, we used a PP Systems accumulation chamber (SRC-1), connected to a portable
202 CO₂ analyser (EGM-4) with an internal pump and rechargeable NiMH battery. The analyser logs CO₂ flux and
203 concentration, and the outlet could be connected to a bag to collect soil gas samples (Lee et al., 2016). The
204 analyser automatically calculates fluxes based on the rise in concentration, for which we specified a linear fitting.
205 We assume there is a linear increase in CO₂ concentration within the cylindrical chamber volume due to
206 constant gas flux. The rate of change in CO₂ concentration over the chamber area (calculated over two minutes
207 for the EGM-4, unless fluxes are high), multiplied by the chamber height then gives the CO₂ flux (Chiodini et
208 al., 1998). Non-linear results generate an error while recording, but wherever all concentration data were saved
209 they have also been checked manually to ensure linear increases in CO₂ concentrations.

210

211 **2.1.3 Tedlar bags**

212 The Tedlar bags used for CO₂ collection and analyses are of impermeable and flexible polyvinyl fluoride, with
213 a plastic valve. Samples in ice caves and warm ground were collected by attaching a bag either to the outlet of
214 the accumulation chamber used for CO₂ flux measurements, or to the outlet of a pump box being used to
215 collect copper tube samples. For lava lake plume and summit fumarole samples, we used 100 mL syringes to
216 draw in air and expel it into the valve, repeating the process several times for each bag, with two samples also
217 collected via a pump box and the outflow of a MultiGas instrument. These samples are expected to contain a
218 significant proportion of ambient air. Clean ambient air and ambient air next to Lower Erebus Hut (LEH) were
219 also collected using a syringe, while ambient air at Tramway Ridge and within caves were collected by

220 connecting to a pump. Samples were analysed with the isotope ratio spectrometer set up at LEH, usually within
221 48 hours of collection (section 2.2).

222 2.2 Isotope ratio infrared spectrometer

223 Carbon dioxide isotope ratios were measured using a tunable-laser isotope ratio infrared spectrometer (IRIS);
224 specifically, the Thermo-Fischer Delta Ray. As in a conventional closed-path infrared spectrometer, the
225 sample gas is passed into an internal cell where it absorbs infrared radiation and the resulting energy spectrum
226 is measured. The absorption wavelengths shift according to the carbon and oxygen isotopes involved, such
227 that peaks on the measured spectrum reflect the proportions of these isotopes. For the Delta Ray, a tunable-
228 laser inside the instrument is the radiation source, targeting the 4.3 μm absorption band. Fitting parameters,
229 including the peaks to be fit, can be specified, and the software uses the HITRAN database (Rothman et al.,
230 2013) as a reference; we used the default settings for CO_2 in air. Using the sizes of and shifts in absorption
231 peaks, the built-in software, Qtegra, calculates the isotope ratios of the sample. The results are referenced to
232 calibration gases of a known composition, which were connected to reference gas intakes and diluted with
233 zero air by the instrument to match the sample concentrations.

234 The instrument was set up inside a hut at Lower Erebus Hut field camp (LEH, elevation approx. 3400 m,
235 ambient air pressure approx. 630 bar). Tedlar bags were connected to the sample intake via tygon tubing and
236 a supplied steel capillary, generally following procedures described by Fischer and Lopez (2016). The sample
237 was pumped into the cell by an internal vacuum pump. To maintain internal cell pressure at the required
238 100.0+/-0.1 mb, an altitude modification was required, in the form of a valve that constricted the tubing
239 between the pump and cell port. For samples containing over 3500 ppm CO_2 , dilution was carried out by
240 adding CO_2 -free air directly from a cylinder into the bags via tygon tubing. Starting concentrations were
241 estimated from the volume change after dilution, or measured using the Delta Ray before dilution. Due to the
242 possibility of contamination by ambient air during dilution, air sampled near the hut, which is shifted to
243 lighter carbon isotope ratios due to emissions from the stove used for heating, is also reported. Samples were
244 referenced to a Thermo Fisher reference gas with isotope ratios of $-27.2 \pm 2 \text{‰}$ $\delta^{18}\text{O}$ and $-27.8 \pm 2 \text{‰}$ $\delta^{13}\text{C}$.

245 2.3 Laboratory analyses

246 Gas compositional analyses were conducted for copper tube, Giggenbach bottle, and some vial samples, in
247 the Volatiles Laboratory at the University of New Mexico following techniques most recently reported by Lee
248 et al.(2017). Splits of the same sample were used for gas chromatography (GC) and quadrupole mass
249 spectrometry. We used a Gow Mac GC with a discharge ionization detector, using a 5Å molecular sieve
250 column with helium as the carrier gas, providing CO_2 , $\text{Ar}+\text{O}_2$, N_2 , CH_4 , and CO . A Pfeiffer QMS was used in
251 dynamic mode to measure He, Ar, O_2 , and N_2 . A liquid nitrogen trap was used to freeze out most water
252 before QMS analyses; but as oxygen measurements from the QMS may still be affected by water the results
253 given here use N_2 from the GC, and Ar and O_2 calculated as follows:

$$254 \text{Ar}_{\text{reported}} = \text{Ar}_{\text{QMS}}/\text{N}_{2\text{QMS}} * \text{N}_{2\text{GC}}$$

$$255 \text{O}_{2\text{reported}} = (\text{Ar}+\text{O}_2)_{\text{GC}} - \text{Ar}_{\text{reported}}$$

256 Helium amounts in several samples were above background atmospheric measurements, but due to the
257 possibility of interference from hydrogen affecting apparent helium content during QMS analyses, these data
258 are not used in our interpretations. Argon isotope ratios were obtained by using the QMS to measure masses

259 36, 38, and 40 in static mode, after a liquid nitrogen trap and a charcoal trap at 550°C, following Lee et al.
260 (2017).

261 Compositional analyses showed variability between copper tube samples collected from the same soil probes
262 at almost the same time, which may be due to variations in the level of air contamination. Two possible
263 causes of air contamination are: (1) that air was mixed in during crimping of copper tubes, (2) that cave air,
264 rich in CO₂ and otherwise similar to outside air, is held in the shallow soil and gravel and pumped into our
265 sample set up, but is displaced by intermittent puffs of pristine gas. Most break seal sample splits for nitrogen
266 isotope analyses were therefore prepared from the same copper tubes analysed by GC-QMS. The copper tube
267 was attached to a valve which connected to the vacuum line and a borosilicate break seal at a three-way
268 connection. After evacuating the break seal, a split was taken for GC-QMS analyses, and the copper tube was
269 opened a second time to the break seal to increase the sample pressure, before torching it off. Nitrogen
270 isotope analyses were conducted by isotope ratio mass spectrometry, following de Moor et al. (2013). Air
271 standards in glass break seals were run every 3-4 analyses as references to correct raw values ($\delta^{15}\text{N} = 0\text{‰}$). A
272 blank was also run for each sample or air standard before breaking it, with the peak areas subtracted from
273 those subsequently measured in the sample or standard run. The blank-corrected air values were subtracted
274 from the blank-corrected sample values. Reported errors are given in 1 s.d. over 4-6 peaks. Although the
275 number of peaks for calculations varies between samples, the same peak numbers were used for the blank
276 corrections and the air standard associated with each sample. Samples collected in 2012 were analysed for
277 carbon and some noble gas (³He/⁴He and ⁴He/²⁰Ne) isotope ratios at the University of Tokyo using the
278 methods outlined in previous work (Sano et al., 2008).

279

280 3. Results

281

282 3.1 Gas chemistry

283 Gas analyses from the GC-QMS (Table 1) show that most samples have air-like compositions. The main
284 differences between samples are in their CO₂, O₂, and N₂ contents (Fig. 3). Hydrogen (H₂) and methane
285 concentrations are below 0.1%, and CO below 0.2%. Other hydrocarbons may be present, and a fuel-like
286 smell was observed in parts of Warren Cave, but these cannot be measured using our current methods. CO₂
287 contents are up to 2.9%, with four samples containing less CO₂ than ambient air on Erebus. The lowest
288 CO₂/CO ratio measured is 0.5, at Ice Tower Ridge in 2016, while at other sites, CO is not detectable.

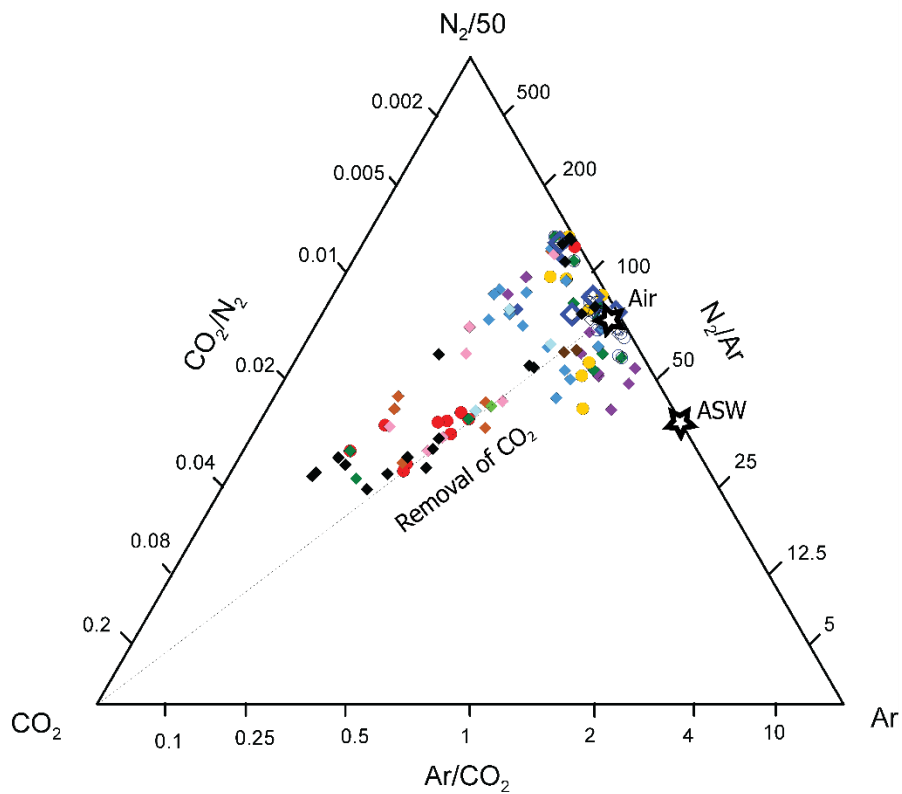
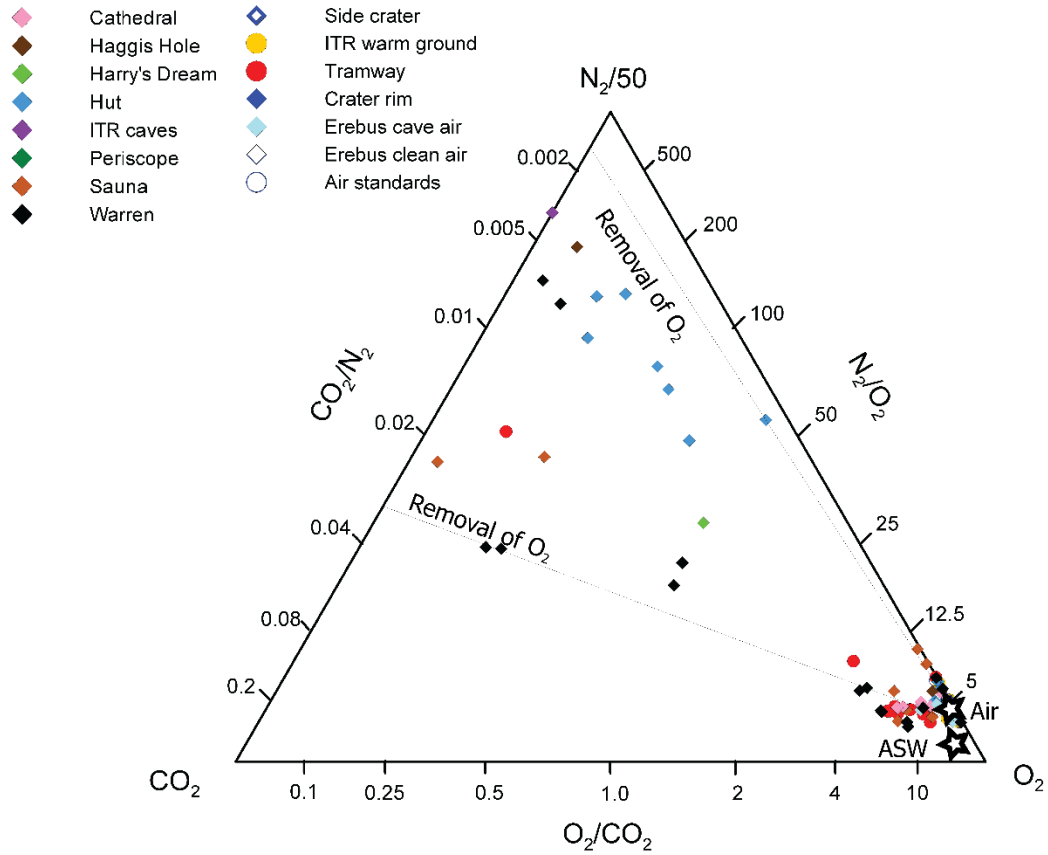
289

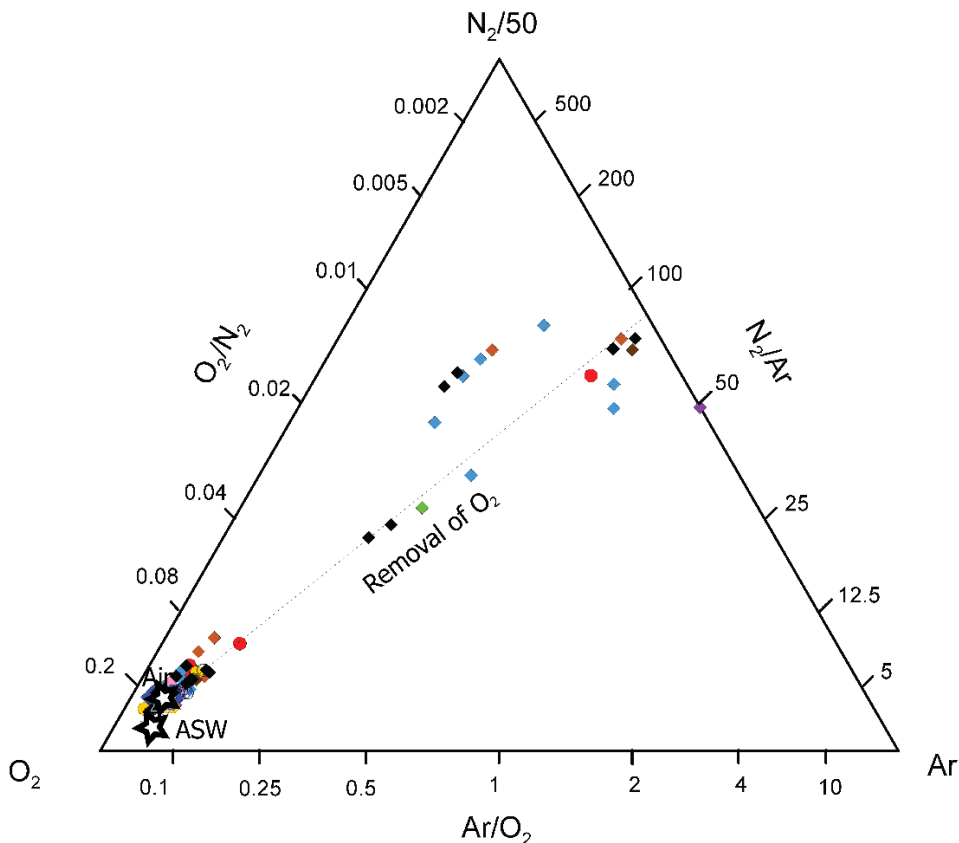
290 Of the potentially air-derived components, nitrogen varies from about 76% to up to 99%, while oxygen is
291 typically close to or less than 21% down to <1% (with a few samples up to 24%), and argon from 0.5% to
292 1.3%. There is no clear trend in the relationship between these components; low oxygen samples occur across
293 a range of N₂/Ar ratios. High CO₂ concentrations occur both in samples where N₂/Ar and N₂/O₂ ratios
294 resemble air, and in those that are oxygen-poor.

295

296 The samples taken at Hut Cave show that measurements at one site may vary significantly, and as mentioned
297 in section 2, analyses of duplicate copper tubes from the same sampling setup can show differing degrees of
298 air contamination. This includes sites where gas flow out was known to have high CO₂ flux (e.g. Tramway,
299 Sauna) or to be concentrated (such as sites at Ice Tower Ridge and Hut Cave), and we thus consider this to be
300 a result of unsteady flow, at least in some cases, rather than contamination during sampling.

301



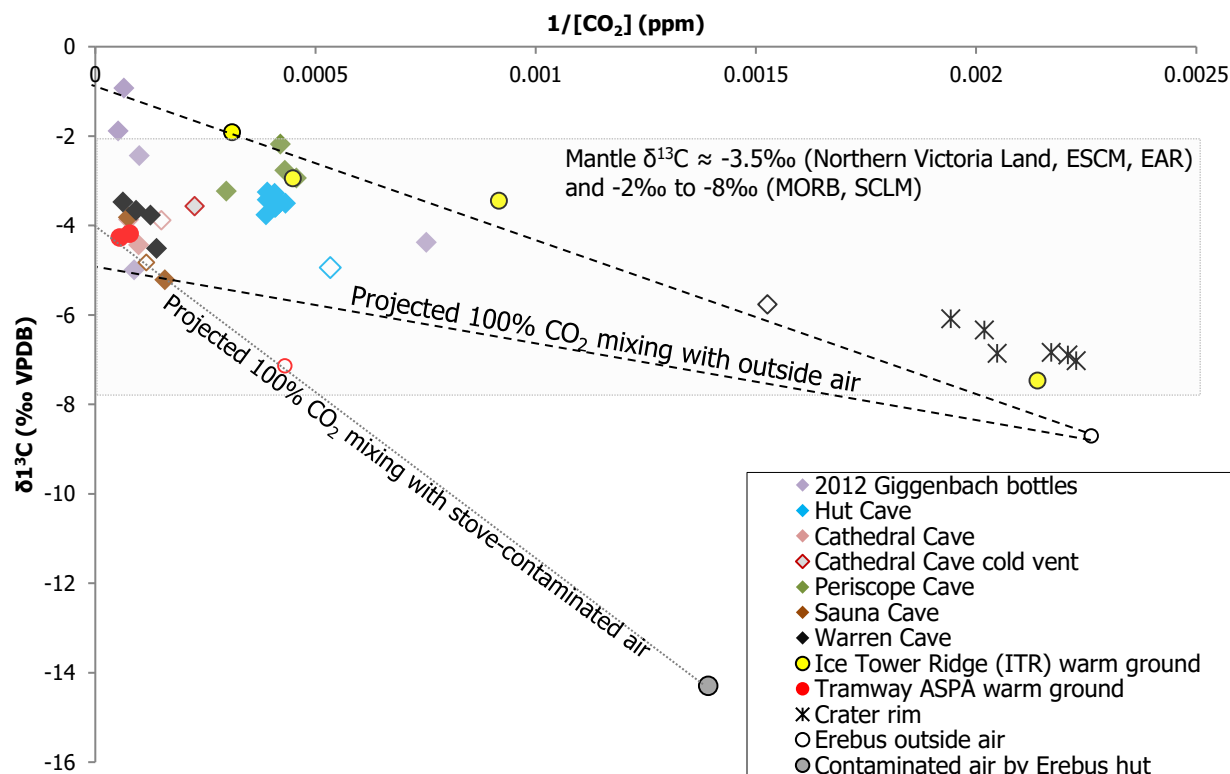


303
304 **Figure 3.** Ternary plots of data measured in 2012, 2015, and 2016 field seasons by GC-QMS. Labels on
305 projected mixing lines are as follows; ‘removal of O_2 ’ is relative to air-like initial gas compositions, and
306 ‘removal of CO_2 ’ is relative to a hypothetical mantle-derived gas: (a) CO_2 - N_2 - O_2 : note CO_2/N_2 of up to 0.03,
307 compared to starting compositions of air (0.0005) and ASW (0) values and elevated N_2/O_2 in several samples
308 across a range of CO_2 contents, (b) CO_2 - N_2 - Ar : as with plot (a), there is a range in CO_2 that appears to be
309 independent of N_2 and Ar content (c) O_2 - N_2 - Ar : the primary variation is again in O_2 content. Also note,
310 generally, the contrast in CO_2 content between ITR warm ground and Tramway – samples from Cathedral,
311 Harry’s Dream, and Sauna also have lower N_2/CO_2 compared to Hut Cave, Side Crater, the ITR caves, and
312 Haggis Hole, while Warren Cave has a greater range of values.

313
314

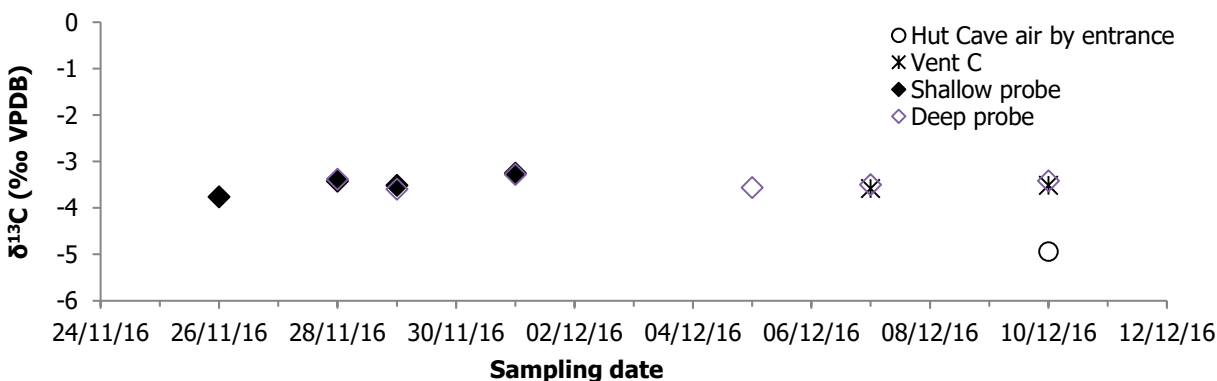
315 3.2 Carbon and oxygen isotope ratios

316
317 Carbon isotope ratios (Fig. 4) are mostly between -2‰ and -6‰. Mixing lines through clean Erebus air or air
318 contaminated by stove exhaust from the hut generally project to a range of values between -1‰ and -4‰ at
319 pure CO_2 , and one 2012 sample from Tramway (Table 3) projects to -4.8‰ on a mixing line with 2016
320 outside air. Crater rim samples are similar across sampling methods (pump, MultiGas, syringe), indicating no
321 systematic fractionation, as also found by Schipper et al. (2017). The time series of samples collected into
322 Tedlar bags at Hut Cave (Fig. 5) shows very consistent results, both in concentration and in $\delta^{13}C$ values.

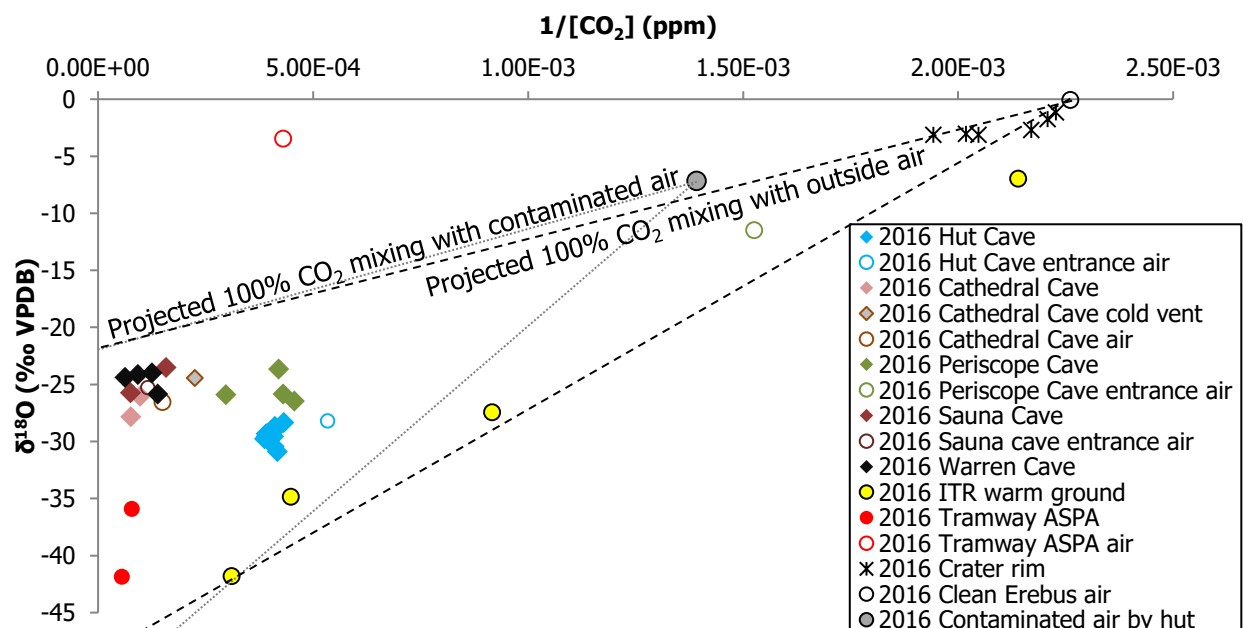


323
 324 **Figure 4.** Carbon isotope ratios from Erebus 2016 field season Tedlar bag samples measured by Delta Ray,
 325 and from 2012 measured by conventional IRMS. Hollow symbols represent ambient air sampled at cave
 326 entrances or above warm ground area. Mantle $\delta^{13}\text{C}$ are: -3.5‰ for Northern Victoria Land Subcontinental
 327 Lithospheric Mantle (Correale et al., 2017), European Subcontinental Mantle (Bräuer et al., 2016), and East
 328 African Rift (Lee et al., 2016); -2 to -8‰ SCLM-derived xenoliths (Cartigny, 2005); $-5 \pm 3\text{‰}$ MORB (Fischer
 329 and Chiodini, 2015). Note that the measured data do not plot on a single mixing line and the heaviest values
 330 of around -1‰ are outside of the potential mantle range.

331
 332
 333 Oxygen isotope ratios of CO_2 measured by Delta Ray (Fig. 6) also vary with $\delta^{13}\text{C}$, and lighter oxygen isotope
 334 ratios are associated with warm ground areas, while cave vent samples are mostly in the -20 to -30‰ range.
 335



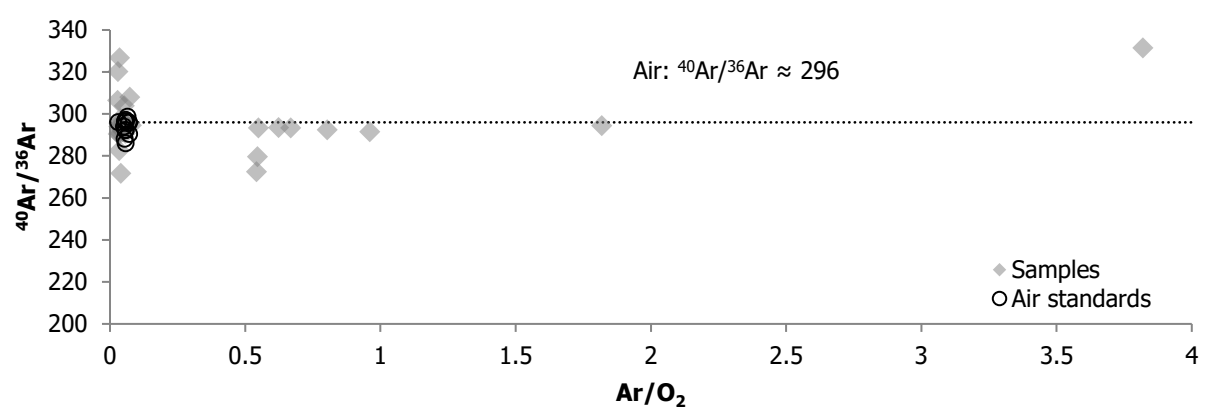
336
 337 **Figure 5.** Time series of carbon isotope ratios collected in Tedlar bags in Hut Cave, measured by Delta Ray,
 338 showing relatively consistent measurements over time and between vents. These are the same data shown in
 339 Figure 4 for Hut Cave and the ambient air at Hut Cave entrance.



340
 341 **Figure 6.** Oxygen isotope ratios of CO₂ from Erebus 2016 field season measured by Delta Ray. Symbols as
 342 for Figure 4. The lightest values are associated with warm ground areas and mixing with air is apparent in
 343 samples from ITR warm ground
 344

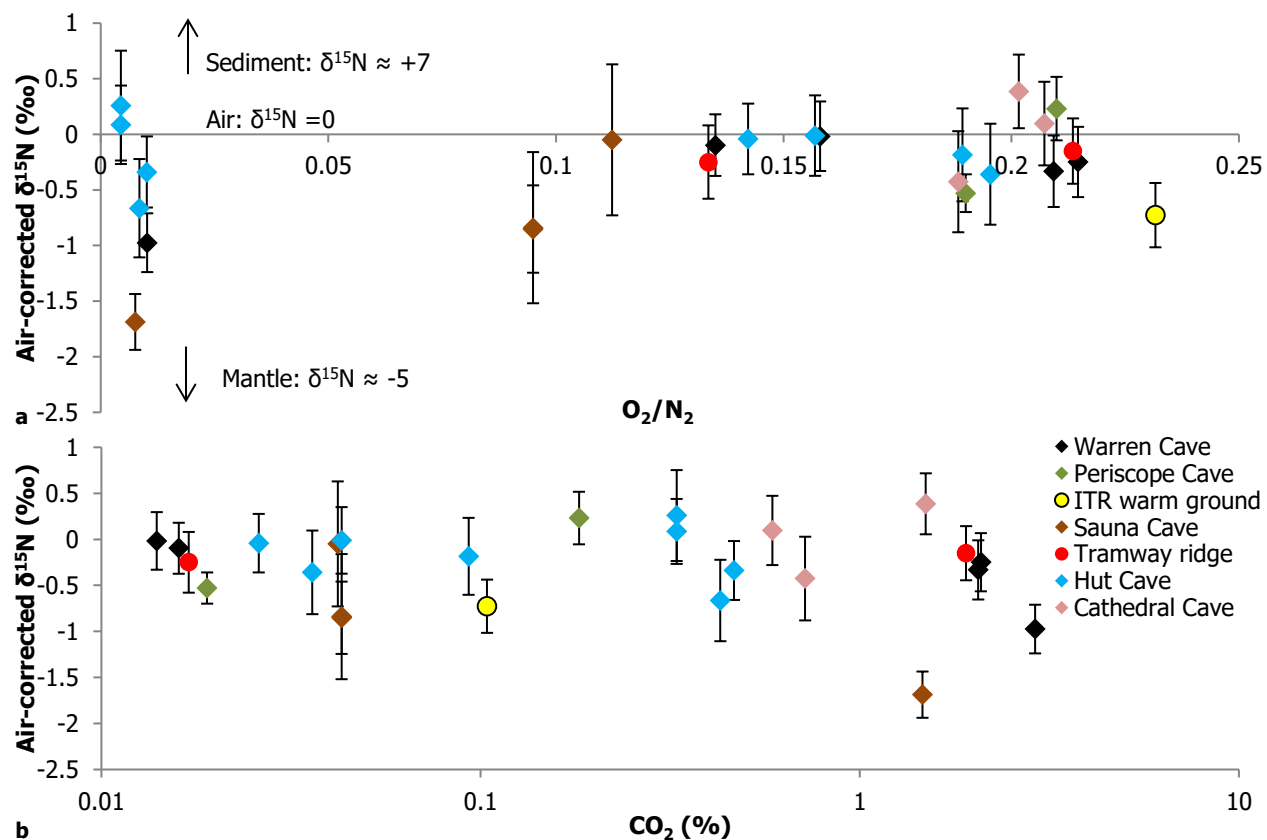
345 Argon isotope ratios (Fig. 7), measured on the QMS, range from 272 – 331, which is generally in the range
 346 measured for our internal air standard (⁴⁰Ar/³⁶Ar = 286 – 308). The highest value of 331 corresponds to a
 347 sample from Hut Cave (HUT-shallow-14), which has the highest N₂/Ar ratio and very little O₂.
 348

349 Nitrogen isotopes range from -1.7 – +0.4‰ vs air, with 1 s.d. up to 0.6‰ (Table 1, Fig. 7), after recalculating
 350 the variance to include standard deviations of air standards used to correct measured raw values from IRMS.
 351 The lightest of these values are outside of the range expected for air. Helium isotope ratios (Table 2) are just
 352 above those expected for air, with a range of 1.03 – 1.18 R_a, whereas ⁴He/²⁰Ne closely resemble air values of
 353 0.318 (Sano and Wakita, 1985).
 354
 355



356
 357 **Figure 7.** ⁴⁰Ar/³⁶Ar from 2015 and 2016 samples and laboratory air, measured by QMS. Note that variability
 358 in ⁴⁰Ar/³⁶Ar does not seem to correlate with Ar/O₂, with higher ⁴⁰Ar/³⁶Ar occurring in samples with
 359 relatively high and low O₂ contents.

360



361

362

363

364

365

366

367

368

Figure 8. Nitrogen isotope ratios from IRMS, plotted against (a) O_2/N_2 ratios measured by GC-QMS; (b) CO_2 (%) measured by GC-QMS. Symbols as for Figure 4. The errors bars of the majority of samples fall within the range for air, with the clearest exceptions being samples from Sauna and Warren caves, and ITR warm ground. There does not appear to be a clear trend but the lightest $\delta^{15}\text{N}$ are associated with higher CO_2 and low O_2/N_2

369 **Table 1.** Summary of gas data from laboratory analyses (GC-QMS and IRMS); italics indicate ambient air samples (not pumped); < indicates peaks
 370 visible on GC but amounts below software detection thresholds; *duplicate Cu tubes from the same sample setup as the previous sample; ¹Known or
 371 probable helium contamination from GC (copper tubes) or lab air (vials), or possible interference from hydrogen in QMS analyses

Type	Sample ID	Site	Gas composition (vol %) from GC-QMS								QMS (static) ⁴⁰ Ar/ ³⁸ Ar	IRMS		
			CO ₂	He	H ₂	Ar	O ₂	N ₂	CH ₄	CO		Sample ID	δ ¹⁵ N	1 s.d.
2012 Cu tubes	EBG-2b	Haggis Hole	0.37	0.0017	0.00051	1.28	0.15	98.20	0.00073	<				
	EBG-20	Sauna	2.09	0.0023	0.0012	1.15	0.16	96.57	0.00054	0.016				
	EBG-14	Tramway	1.08	0.0013	<	0.87	22.33	75.72	0.0011	<				
	EBG-13	Warren v2	0.60	0.0024	0.00044	1.19	0.23	97.99	<	<				
	EBG-9	Warren v5	1.84	0.0013	<	0.90	21.48	75.78	<	<				
	EBG-10 ¹	Warren v6	0.06	NA	<	0.89	23.42	75.62	<	<				
	EBG-12	Warren v7	2.09	0.0013	<	0.86	23.75	73.30	<	<				
	EBG-11	Warren v8	0.58	0.0015	0.00045	1.23	0.10	98.09	<	<				
2012 Giggenschbach bottles w. caustic	EBG-11	Warren v8	0.00	0.0016	<	1.03	13.99	84.98	0.00017	<				
	EBG-9	Warren v5	0.00	0.0013	<	1.06	13.78	85.17	<	<				
	EBG-12	Warren v7	0.00	0.0017	<	1.04	13.79	85.17	<	<				
	EBG-13	Warren v2	0.00	0.0014	<	1.02	14.62	84.36	<	<				
	EBG-15	Harry's Dream	0.00	0.0010	<	1.05	13.62	85.33	<	<				
	EBG-20	Sauna	0.00	0.0016	<	1.03	13.97	85.00	0.00031	<				
EBG-14	Tramway	0.00	0.00079	<	0.97	13.64	85.39	0.0017	<					
2012 Air standards	<i>Crest air</i>	<i>Sandia crest</i>	<i>0.05</i>	<i>0.00096</i>	<i>0.00061</i>	<i>0.97</i>	<i>17.67</i>	<i>81.31</i>	<	<				
	<i>Crest air</i>	<i>Sandia crest</i>	<i>0.06</i>	<i>0.0015</i>	<	<i>0.97</i>	<i>17.56</i>	<i>81.42</i>	<	<				
	<i>Crest air</i>	<i>Sandia crest</i>	<i>0.05</i>	<i>0.0012</i>	<	<i>0.96</i>	<i>17.62</i>	<i>81.37</i>	<	<				
	<i>Crest air</i>	<i>Sandia crest</i>	<i>0.05</i>	<i>0.0014</i>	<	<i>0.94</i>	<i>17.46</i>	<i>81.54</i>	<	<				
2015 Cu tubes	TR1	Tramway	1.47	0.0020	0	1.23	0.41	96.89	0.0020	0.0010				
	HUT1	Hut	0.44	0.0019	0	1.40	0.34	97.82	0.0010	0.0020		HUT-2B_2015	-	0.433
	SCR1	Side Crater	0.01	0.0022	0	1.04	18.37	80.58	0	0		SCR-2B_2015	-	0.585
	ITR-B-1 ¹	Shooting gallery 'blob'	0.05	NA	0	0.95	20.06	78.93	<	0				
	ITR-KM-1	Shooting gallery main	0.13	0.0013	0	0.83	20.36	78.67	<	0				
	ITR-UWG-11	ITR upper warm ground	0.02	0.0013	0.0010	0.99	12.56	86.43	0.0010	0.0020		ITR-UWG-12_2015 B	0.05	0.612
	DDNOS	Hollow near Derodrome	0.15	0.0009	0.0000	1.17	20.89	77.79	<	<				
	ITR-UWG-6	ITR upper warm ground	0.41	0.0012	0	1.42	21.11	77.06	<	<				
	ITR-H-1	Heroin	0.14	0.0013	0	1.01	21.24	77.61	<	<		ITR-H-2B_2015	-	0.316
	ITR-LWG-1	ITR lower warm ground	0.29	0.0006	0	1.20	21.35	77.15	<	<				
	ITR-B-6	Shooting gallery 'blob'	0.36	0.0008	0	1.98	0.00	97.66	<	0.0010				

												ITR-B-7A_2015	0.21	0.122
												ITR-B-7B_2015	-	0.303
	ITR-P-1	Passage by Shooting	0.13	0.00058	0	1.46	20.58	77.83	<	0.0020				
	ITR-TOM-1	Tomato cave	0.06	0.00064	0	1.38	20.91	77.65	<	<				
	ITR-B-16	Shooting gallery 'blob'	0.23	0.00072	0	1.27	21.15	77.35	<	<				
	ITR-B-11	Shooting gallery 'blob'	0.23	0.00059	0	1.23	20.41	78.13	<	<				
	ITR-B-13	Shooting gallery 'blob'	0.23	0.0011	0	1.17	20.94	77.65	<	<				
	ITR-B-A	Shooting gallery 'blob'	0.23	0.00060	0	1.10	19.88	78.79	<	<				
	ITR-UWG-1	ITR upper warm ground	0.23	0.00056	0	1.18	19.80	78.80	<	<				
	ITR-B-12	Shooting gallery 'blob'	0.23	0.00058	0	1.29	18.96	79.52	<	<				
	HUT-3-2015 ¹	Hut	0.43	NA	<	0.67	0.83	98.06	0.0010	0.0010	292.36	HUT-3_2015	-	0.321
	TR-3-2015*	Tramway	0.02	0.0013	0.0010	0.71	11.69	87.58	0.0020	0.0030	294.97	TR-3_2015	-	0.241
												TR-2B_2015	-	0.278
	ITR-KP-2 2015	Shooting gallery	0.23	0.0014	0.001	0.59	19.11	80.06	<	<	290.42			
	ITR-B-8 2015	Shooting gallery 'blob'	0.34	0.0018	<	0.59	19.18	79.89	<	<				
	ITR_UWG_13 2015 ¹	ITR upper warm ground	0.01	NA		0.63	15.88	83.47		0.0010				
	SCR_3 2015	Side Crater ice tower	0.05	NA		0.59	18.63	80.71		0				
2015 Giggenbach bottles	LEH air 9Dec 15	LEH	0.05	0.0016	0	1.16	18.28	80.51	0	0				
	TR6 ¹	Tramway	1.01		0	0.92	19.04	79.03	0.0010	0				
	ITR-LWG	ITR lower warm ground	0.09	NA	0	0.92	19.37	79.61	0	0				
	SCR8	Side Crater	0.16	0.0025	0.0010	0.89	19.29	79.66	0	0				
	SCR9 ¹	Side Crater	0.05		0	0.88	19.78	79.28	0	0				
LEH air 10dec15	LEH	0.04		0	0.87	19.30	79.78	0	0					
2015 air standards	Johnson field air	Johnson field	0.03	0.0005	0	1.23	16.43	82.31	0	0				
	Johnson field air	Johnson field	0.04	0.0005	0	1.12	18.21	80.63	0	0				
	Johnson air	Johnson field	0.03	0.0006	0	1.18	17.44	81.34	0	0				
	Johnson air	Johnson field	0.03	0.0006	0	1.15	17.64	81.18	0	0				
2016 Cu tubes	HUT-1	Hut	0.11	0.0021	0	0.79	13.71	85.39	0	0	303.82			
	Hut-2*	Hut	0.58	NA	<	0.75	1.41	97.25	0	0	279.56			
	HUT-7	Hut	0.39	0.0016	0	0.54	16.70	82.38	0	0	320.09			
	HUT-1-Deep	Hut	0.39	0.0014	0	0.68	17.03	81.89	0	0	326.74			
	HUT-7-Deep	Hut	0.38	0.0014	0	1.26	15.67	82.69	0	0	308.02			
	HUT-14-Shallow	Hut	0.61	0.0018	0	1.56	0.43	97.40	0	0	331.43			
	HUT-Shallow_15*	Hut	0.47	0.0016	0.0020	0.66	0.99	97.87	0.0020	0.0010		HUT-Shallow-15_2016	-0.338	0.236
	HUT_Shallow_16*	Hut	0.04	0.0018	0	0.63	16.24	83.09	0.0010	0		HUT-Shallow-16_2016	-0.358	0.322
	HUT-11-Deep	Hut	0.06	NA	0	1.05	15.83	83.05	0	0.0030	294.59			
	HUT-21-Deep ¹	Hut	0.11	NA ¹	0.0070	1.29	1.64	96.89	0	0.0020	272.50			
	HUT-22-Deep*	Hut												
	HUT_deep_23*	Hut	0.33		0	0.80	0.44	98.43	0.0010			HUT-deep-23A_2016	0.086	0.266
												HUT-deep-23B_2016	0.258	0.349
		HUT-27-Deep	Hut									287.29		

	HUT_deep_28*	Hut	0.04	0.0010	0.64	13.47	85.84	0.0010	0.0020		HUT-deep-28_2016	-	0.267	
	HUT-C-1	Hut - back	0.15	0.0026	<	1.11	20.91	77.82	<	0.0040				
	HUT-C-2* ¹	Hut - back	0.09	NA	0.0010	0.61	15.80	83.49	0.0020	0.0010	HUT-C-2_2016	-	0.297	
	HUT-C-4*	Hut - back	0.03	0.0019	0	0.66	12.36	86.95	0.0010		HUT-C-4_2016	-	0.245	
	CAT-A-1 ¹	Cathedral	1.49	NA	0.0010	0.67	16.42	81.41	0.0010	0.0010	CAT-A-1_2016	0.38	0.246	
	CAT-A-2*	Cathedral	0.72	0.0014	<	0.68	15.63	82.97	0.0010	<	CAT-A-2_2016	-	0.322	
	CAT-B-1 ¹	Cathedral	0.59	NA	0.0010	0.58	16.97	81.86	0.0020	<	CAT-B-1_2016	0.09	0.27	
	CAT-B-4*	Cathedral	0.10	0.0019		0.64	14.51	84.75						
	ITR-UWG-1	ITR upper warm ground	0.10	0.0020	0.0010	0.73	18.61	80.34	0.0010	0.21	294.84			
	PER-A-2 before torching	Periscope	0.02	0.0018	0.0010	0.59	15.87	83.51	0.0010	0.0010	294.17	PER-A-2_2016	-	0.231
	PER-B-2 before torching	Periscope	0.18	0.0017	0.0010	0.49	17.23	82.09	0.0010	0	306.44	PER-B-2_2016	0.23	0.229
	Sauna-A-1	Sauna hot vent	0.04	0.0014	0.001	0.64	10.03	89.28	0.0020	<	293.98	Sauna-A-1_2016	-	0.481
	Sauna-A-2*	Sauna hot vent	1.46	0.0018	0.0010	0.68	0.73	97.12	0.0010	0.0020	291.57	Sauna-A-2_2016	-	0.183
	Sauna-B-1 ¹	Sauna cool vent	0.10	NA	<	0.61	16.35	82.94	<	0				
	Sauna-B-3* ¹	Sauna cool vent	0.04	NA	0.0010	0.68	8.61	90.66	0.0010	0.0010	294.55	Sauna-B-3A_2016	-	0.393
											Sauna-B-3B_2016	-	0.281	
	Warren entrance air	Warren	0.82	NA	0.001	0.56	17.18	81.43	<	<	295.64	ITR-UWG-1_2016	-	0.219
	WAR-v6-1	Warren	2.05	0.0013	0.001	0.56	16.86	80.53	0.001	<	293.97	WAR-v6-1_2016	-	0.246
	WAR-v6-2* ¹	Warren (v6 2012?)	0.05			0.61	18.01	81.32			291.13			
	WAR-vT-1	Warren far back	2.81	0.0015	0.0020	0.61	1.11	95.47	0.001	0.0010	293.41			
	WAR-vT-2*	Warren far back	2.09	0.0020	<	0.64	17.19	80.08	<	0	293.32	WAR-vT-2_2016	-	0.224
	WAR-vT-3* ¹	Warren far back	0.01	NA		0.66	13.55	85.77			291.60	WAR-vT-3_2016	-	0.225
	WAR-CD-1	Warren icy chamber	2.90	0.0013	0.0010	0.61	0.98	95.51	0.0010	0.0010	293.46	WAR-CD-1_2016	-	0.121
	WAR-CD-2* ¹	Warren icy chamber	0.02	NA	0	0.66	11.81	87.50			290.74	WAR-CD-2_2016	-	0.506
	TRAM-A-1	Tramway	1.51	0.0012	0.0020	0.64	16.07	81.77	0.0020	<	295.62			
	TRAM-A-4*	Tramway	1.20	0.0012	0.0020	0.88	17.26	80.64	0.0010					
	TRAM-B-1	Tramway	1.91	0.0015	0.0010	0.59	17.16	80.34	0.0090	<	290.21	TRAM-B-1_2016	-0.15	0.221
2016 air standards	Lab air	In lab	0.10	0.0025	0	1.31	16.58	82.01	0	0	307.89			
	Lab air	In lab	0.11	0.0017	0.001	1.08	16.84	81.96	0	0				
	repeat	In lab	0.07	0.0017	0.001	1.08	16.66	82.19	0	0				
	Johnson field air	Johnson field	0.08	0.0014	0	1.05	18.46	80.41	<	0				
	Johnson field air	Johnson field	0.08	0.0025	0	1.00	18.65	80.27	<	0				
	Johnson field air	Johnson field	0.08	0.0021	<	0.93	16.59	82.40	<	0				
	Lab air	In lab	0.10	0.0033	0	0.96	16.52	82.42	0	0				
	Johnson field air	Johnson field	0.06	0.0015	0	1.10	15.68	83.15	0	0	295.96			
	Johnson field air	Johnson field	0.06	0.0023	<	1.04	16.23	82.67	<	0	298.60			
	Johnson field air	Johnson field	0.06	0.0016	0	0.98	16.98	81.98	0	0	286.01			
	Lab air	In lab	0.06	0.0050	0	0.56	18.61	80.77	<	0	296.08			
	Lab air	In lab	0.08	0.0040	0	0.98	17.63	81.31	0	0	291.57			
	Johnson field air	Johnson field	0.06	0.0017	0	1.02	17.18	81.74	0	0	296.37			
	Johnson field air	Johnson field	0.06	0.0020	<	1.01	17.33	81.60	<	0	292.25			

	<i>Johnson field air</i>	<i>Johnson field</i>	0.07	0.0015	0	1.03	16.13	82.77	0	0
	<i>Johnson field air</i>	<i>Johnson field</i>	0.05	0.0023	0	1.10	16.12	82.72	0	0
	<i>Johnson field air^d</i>	<i>Johnson field</i>	0.04	NA		0.70	17.89	81.29		
2016 vials ¹	<i>HUT-entrance</i>	<i>Hut back</i>	0.38	0.0013	0.0010	0.67	16.58	82.36	0	0.0030
	<i>CAT_CaveAir</i>	<i>Cathedral</i>	0.94	0.0037	0.001	0.58	18.07	80.40	0	0.0030
	CAT_CV	Cathedral cold vent	0.78	0.0025	0.0010	1.08	16.18	81.95	0	0.0030
	<i>Clean air by Cathedral-</i>	<i>Outside cave</i>	0.11	0.0019	0	0.93	23.18	75.78	0	0.00
	TRAM-A-5	Tramway	1.71	0.0028	0.0070	0.98	18.04	79.26	0	0.0020
	TRAM-B-5	Tramway	1.82	0.0052	0.0010	1.02	17.11	80.04	0.0020	0.0030
	<i>Sauna cave air</i>	<i>Sauna entrance</i>	0.31	0.0016	0.0010	0.90	22.91	75.88	0	0.0020
	Sauna-A-5	Sauna hot vent	2.09	0.0012	0.0010	0.76	20.87	76.28	0	0.00098
	Sauna-B-5	Sauna cool vent	0.82	0.0040	0.0020	0.96	20.24	77.96	0	0.0050
	CAT-A-6	Cathedral	1.49	0.0015	0.0010	1.02	16.58	80.89	0	0.0040
	CAT-B-5	Cathedral	1.30	0.0019	0.0020	1.01	16.32	81.35	0	0.0040
	ITR-UWG 30 Nov '16 (QMS)	ITR upper warm ground	0.14	0.0012	0.0010	0.64	23.01	76.20	<	0.0030
	WAR_CD_5_vial	Warren icy chamber	0.07	0.0018	0	0.69	16.48	82.75	0	0
	Sauna_A_good	Sauna hot vent	1.32	0.011	0.0010	0.60	17.29	80.77	<	0.0050
	<i>Low pump site 17:15</i>	<i>Low pump site</i>	0.35	0.011	0.0010	0.69	16.73	82.21	0	0.0020
	<i>Low pump site 17:00</i>	<i>Low pump site</i>	0.08	0.013	0	0.67	16.92	82.32	0	0
	<i>Low pump site 17:06</i>	<i>Low pump site</i>	0.10	0.0077	0.0010	1.10	16.43	82.36	0	0.0030
	<i>Rim after exp 17:15</i>	<i>Low pump site</i>	0.08	0.0034	0.001	1.03	16.51	82.37	0	0.0020
	HUT_5_shallow	Hut	0.36	0.0016	0.058	0.98	16.13	82.47	0.0010	0.0020

372 **Table 2.** Helium isotope ratios for Cu tube samples in 2012

Sample location	³ He/ ⁴ He (R _{atm})	⁴ He/ ²⁰ Ne
Harry's Dream	1.10	0.319
Tramway	1.08	0.313
Warren v7	1.05	0.319
Warren v6	1.03	0.316
Warren	1.18	0.320

376 **Table 3.** Erebus CO₂ isotope ratios from analyses by IRMS (2012) and IRIS (Delta Ray, 2016)

Sample ID	Date collected	δ ¹³ C (‰)	δ ¹⁸ O (‰)	[CO ₂] (ppm)
Cathedral				
CAT-cold vent ¹	09/12/2016	-3.57	-24.46	4,440
CAT-cave air ¹	09/12/2016	-3.89	-26.55	6,679
CAT-B-0 ^{1,2}	09/12/2016	-4.43	-26.05	10,210
CAT-A-0 ¹	09/12/2016	-3.87	-27.84	13,150
Harry's Dream ³	2012	-2.44		10,010
Hut cave				
Hut 0 (shallow)	26/11/2016	-3.76	-29.76	2,52
HUT-6 (shallow)	28/11/2016	-3.43	-29.57	2,559
HUT-7 (shallow)	29/11/2016	-3.52	-29.51	2,464
HUT-13 (shallow)	01/12/2016	-3.25	-29.32	2,560
HUT-DEEP-0	28/11/2016	-3.38	-29.31	2,492
HUT-DEEP-1	29/11/2016	-3.60	-29.58	2,452
HUT-DEEP-6	01/12/2016	-3.28	-29.07	2,458
Hut Cave deep site	05/12/2016	-3.56	-29.04	2,438
HUT-DEEP-20	07/12/2016	-3.50	-28.33	2,315
HUT-DEEP-26	10/12/2016	-3.42	-28.68	2,434
HUT-C-0	07/12/2016	-3.59	-30.46	2,441
HUT-C-1 ²	10/12/2016	-3.51	-30.91	2,399
HUT-entrance air	10/12/2016	-4.94	-28.20	1,874
Periscope				
PER-AIR	03/12/2016	-5.77	-11.48	655
PER-A-0	02/12/2016	-2.18	-23.66	2,381
PER-B-0	02/12/2016	-2.77	-25.85	2,324
PER-B-1 ²	03/12/2016	-2.94	-26.46	2,197
PER-A-1	03/12/2016	-3.23	-25.91	3,363
Sauna				
Sauna-A-0 ¹	04/12/2016	-3.82	-25.74	13,275
Sauna-B-0 ¹	04/12/2016	-5.22	-23.51	6,320
Sauna-entrance air ¹	04/12/2016	-4.83	-25.28	8,660
Warren				
Warren v7 ³	2012	-1.89		19,321
Warren v6 ³	2012	-0.93		15,500
Warren ³	2012	-4.38		
WAR-CD-0 ^{1,*}	02/12/2016	-3.77	-23.99	8,000
WAR-v6-0 ^{1,*}	30/11/2016	-3.47	-24.38	15,950
WAR-CD-0 ^{1,*}	02/12/2016	-4.51	-25.85	7,200
WAR-v6-1 ^{1,*}	02/12/2016	-3.66	-24.13	10,800
ITR-UWG				
ITR-UWG	30/11/2016	-7.46	-6.96	467
ITR UWG p63 ²	27/11/2016	-2.95	-34.84	2,231
ITR UWG 'fumarole' probe	30/11/2016	-1.92	-41.80	3,223
ITR-UWG p56	26/11/2016	-3.45	-27.44	1,091
Tramway				
Tramway ³	2012	-4.99		11,386
TRAM-A-0 ¹	05/12/2016	-4.18	-35.91	12,795
TRAM-B-0 ¹	05/12/2016	-4.27	-41.87	18,160
Tramway air	05/12/2016	-7.14	-3.47	2,322
Rim				
Pump site via pump box 11:45	02/12/2016	-7.03	-1.16	448.9
Pump site via MultiGas outflow 12:00	02/12/2016	-6.84	-2.70	460.8
Rim - low pump site 16.50	08/12/2016	-6.86	-3.13	488.4
Rim - low pump site 16.58	08/12/2016	-6.34	-3.04	495.4
Rim - low pump site after explosion 17.15	08/12/2016	-6.90	-1.75	452.9
Rim - low pump site after explosion 17.10	08/12/2016	-6.09	-3.14	514.9
Clean air				
CAT-clean air	09/12/2016	-8.71	-0.08	442.3
Contaminated air outside garage				
Outside air	08/12/2016	-14.30	-7.17	718.4

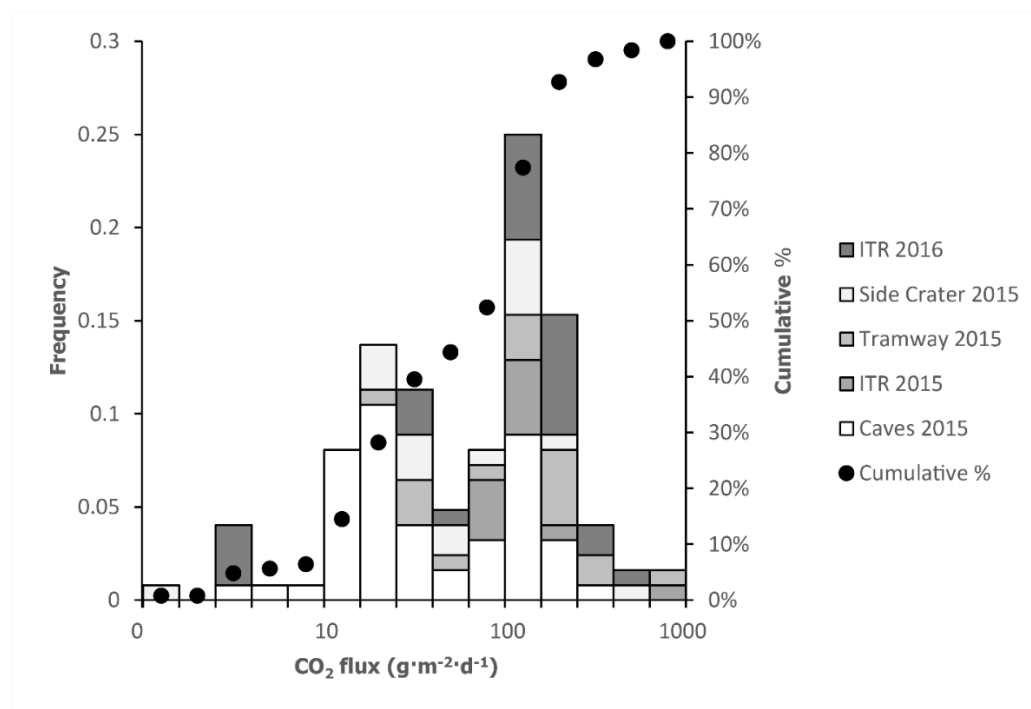
377 * estimated concentration based on dilution volume

378 ¹diluted prior to analysis

379 ²average of repeat measurements

380 ³concentrations for samples analysed by IRMS are from corresponding GC-QMS analyses of Giggenbach bottles

381 **3.3 Carbon dioxide fluxes**



382

383 **Figure 9.** Population distribution of flux measurements in 2015 and 2016 at warm ground and cave sites.
 384 Note peaks at about 20-30 and 100-200 $\text{g}\cdot\text{m}^{-2}\cdot\text{d}^{-1}$, which occur in both cave and warm ground data.

385 Carbon dioxide fluxes measured in caves on Ice Tower Ridge (ITR) and the warm ground areas at ITR,
 386 Tramway, and Side Crater, seem to follow bimodal distributions (Fig. 9). Fluxes were estimated for three
 387 warm ground sites based on their areas (Table 4), but do not include all such sites on the volcano due to time
 388 and access constraints.

389 **Table 4.** Summary of estimated CO_2 fluxes from warm ground areas, showing a good match between data
 390 collected at ITR in 2015 and 2016 despite the small number of samples.

Warm ground site	Mean flux ($\text{g}\cdot\text{m}^{-2}\cdot\text{d}^{-1}$)	No. points	Median flux ($\text{g}\cdot\text{m}^{-2}\cdot\text{d}^{-1}$)	Area (m^2)	Total emissions (CO_2 $\text{t}\cdot\text{d}^{-1}$)
Side Crater	119.6	17	74.88	17453 ¹	2.09
Tramway Ridge	289.8	17	149.5	17500 ²	4.28
ITR (2015)	199.5	11	149.3	9164 ³	1.83
ITR (2016)	195.8	36	154.6	9164 ³	1.79
All measured (2015)	201.5	45	121.0	44117	8.2

391

392 ¹ From map of Side Crater in Panton and Winter (2008) and field observations
 393 ² From satellite imagery and Tramway ASPA map (ASPA No. 175 management plan, 2014)
 394 ³ Estimated from area of Western Crater from handheld GPS walk around limits of warm ground (8834 m^2) –
 395 and steeper upper warm ground areas where flux measurements were taken, estimated using tape measure
 396 (330 m^2).
 397
 398

399 **4. Discussion**

400 These gas data show a number of features, including variations in CO₂ with a range of carbon isotope ratios
401 that cannot be explained solely by mixing; a significant number of samples that appear to be dominated by
402 air; and varying proportions of O₂ and N₂. We focus first on CO₂ content and carbon isotope ratios, to better
403 understand the original source gas composition and modification of isotope ratios. Next, we discuss (section
404 4.2) air entrainment and processes affecting other components in the measured gas, evidence for which are
405 supported by stable isotope data (section 4.3). Finally, we present a model for the interactions taking place
406 within the volcanic edifice to produce the measured gases.

407 **4.1 Carbon dioxide**

408 Vent and diffuse degassing samples typically contain higher concentrations of carbon dioxide than air. The
409 majority of samples have over 2% (2000 ppmv) CO₂, but only range up to 2.9%. In the following section, we
410 consider the carbon isotope ratios associated with these samples, focusing on the source compositions and
411 fractionation processes that result in the measured $\delta^{13}\text{C}$ values and their spatial distribution.

412 **4.1.1 Carbon isotope ratios**

413 Previous carbon isotope analyses of gas at Erebus by Wardell et al. (2003) found a range of $\delta^{13}\text{C}$ of -2.04‰ to
414 -4.61‰. This was interpreted as an enriched signature from a mantle-derived component with $\delta^{13}\text{C}$ of -2.1‰
415 mixed with varying proportions of air. Our measured values overlap with these but have a greater range (-
416 0.9‰ to -5.0‰ before accounting for mixing with air). This matches the $-5\pm 3\%$ typical of MORB (Fischer
417 and Chiodini, 2015), and the -2‰ to -8‰ range of SCLM xenoliths (Cartigny, 2005), so may reflect a mantle
418 source, but the range of values indicates either heterogeneities in the source carbon isotope ratios, or shallow
419 modification. Fractionation affects the carbon isotope ratios of mantle-derived gases as they travel through
420 the crust, interacting with rock, crustal fluids, and surface air. Additional contributions to CO₂ measured at
421 the surface may also come from mixing, such as with biogenic CO₂, although this is likely to be a minor
422 contribution at Erebus.

423

424 The measurements at Hut Cave (Fig. 5) suggest that $\delta^{13}\text{C}$ is stable over short time periods (about 14 days) at
425 both sites (Hut Cave main vent and Hut Cave Vent C), with no notable difference corresponding to sampling
426 depth in the soil (Deep probe, Shallow probe).

427

428 We consider scenarios that could determine the range of carbon isotope ratios observed from a combination
429 of source signatures and subsequent fractionation or other modification. We first rule out the possibility that
430 the CO₂ originates from a heavy $\delta^{13}\text{C}$ end-member. A heavy end-member would need to reflect the original
431 mantle signature and modification in the crust, prior to shallower processes causing fractionation, to lighter
432 values. At Etna, a similarly heavy end-member is attributed to modification by crustal carbonate sediments
433 (D'Alessandro et al., 1997; Correale et al., 2015). Such an influence is unlikely at Erebus, as there is limited
434 evidence for carbonate basement rock in the crust beneath the McMurdo Sound area (Sims et al., 2008;
435 Fielding et al., 2011; Scopelliti et al., 2011; Phillips et al., 2018), so we consider this improbable. It is more
436 likely that the lighter values reflect an original mantle signature close to MORB values e.g. -4.5 ‰, Cartigny et
437 al. (2001); -5 to -8 ‰, Javoy et al. (1986), or Subcontinental Mantle Lithosphere of around -3.5 ‰ (Bräuer et
438 al., 2016; Lee et al., 2017) and modification is a result of shallow fractionation in the crust.

439

440 We also note that there is potential heterogeneity in the mantle source beneath the WARS. The compositions
441 of Erebus lineage lavas indicate HIMU mixed with DMM type mantle, but their mantle source is considered
442 to be heterogeneous (Sims et al., 2008). Correale et al. (2017) report WARS mantle $\delta^{13}\text{C}$ values of -2.5 to -
443 4.5‰ in mantle xenoliths found in Northern Victoria Land. If similar values apply for the Erebus volcanic
444 province mantle, then our measured carbon isotope ratios could be achieved with only minor fractionation.
445

446 However, we do not expect that heterogeneity in carbon isotope ratios at mantle depths could be preserved
447 over very small spatial distances such that distinct $\delta^{13}\text{C}$ values were measured at sites only hundreds of metres
448 apart. We therefore assume a lighter source $\delta^{13}\text{C}$. An initial $\delta^{13}\text{C}$ of -4‰, for example, could cover most of
449 our range of measured values with about +3‰ fractionation. Fractionation processes, such as through
450 magmatic degassing, hydrothermal dissolution, or transport through soil, are the next step in explaining how
451 the measured range of compositions could have been generated.
452

453 Potential influences on the nature and extent of fractionation include (i) the depths and temperatures of
454 shallow degassing magma bodies; (ii) diffusive and advective transport of CO_2 ; and (iii) the presence and
455 temperatures of any hydrothermal systems, which may relate to the presence of magma bodies and water
456 availability (Table 5). We next consider each of these factors, noting that mixing with non-volcanic CO_2
457 sources would require large quantities of CO_2 with distinct $\delta^{13}\text{C}$, and cannot be an important effect here.
458 Although biological and surface air signatures are lighter than mantle, surface air only contributes about 400
459 ppm of CO_2 , and with limited biological activity on Erebus, significant microbial CO_2 would be required to
460 alter the isotope ratios of the projected 100% CO_2 .
461

462 (i) Fluxing of CO_2 through the magmatic column is often invoked to explain high CO_2 emissions
463 from Erebus lava lake (Oppenheimer et al., 2011), so the emissions we measure are likely to be
464 sourced from depth, as well as from shallower phonolite magma bodies. Fractionation by
465 magmatic degassing results in lighter carbon isotope ratios.
466

467 In such a scenario, emissions at Tramway and Sauna cave, and to a lesser extent Cathedral and Warren caves
468 (extrapolated to -3 to -4.5‰ at 100% CO_2), would be fractionated to lighter end-members and derive from
469 shallower sources. With a source $\delta^{13}\text{C}$ likely close to -4‰, little fractionation would be required to explain
470 our lightest values. The upper limit on fractionation by magmatic degassing for basalts is well above this, at
471 around -4‰ (Gerlach and Taylor, 1990; Javoy et al., 1978; Matthey, 1991), though no published data are
472 available for basanite, which is the parent melt at Erebus. While degassing pathways are too small to be
473 resolved, Zandomenighi et al. (2013) do identify larger potential magma bodies at Erebus using seismic
474 tomography. Tramway and Sauna are associated with shallow high velocity zones, i.e. potential hot intrusions,
475 while Hut Cave and Ice Tower Ridge overlie hydrothermal systems or chilled magma bodies. Sources beneath
476 Warren and Cathedral are less clear. The hot intrusions could be a source of gas that has fractionated during
477 magmatic degassing, but this does not account for the heavier $\delta^{13}\text{C}$ at other sites such as Periscope Cave or
478 the crater rim. Another mechanism is required for fractionation to heavier values.

479 (ii) Federico et al. (2010) report significant transport-driven fractionation effects during diffuse
480 degassing of CO_2 that can lead to apparent increases in $\delta^{13}\text{C}$. This is an important consideration,
481 as there can be fractionation of over 4 ‰ in the interaction between CO_2 and air during
482 diffusion into shallow soil layers (Camarda et al., 2007).

483 This is a difficult effect to evaluate, as many factors may contribute to transport-driven fractionation,
484 including the soil type and CO₂ flux, the pump rate and depth of the sample probe, and wind. The latter is
485 most likely to have affected measurements at Ice Tower Ridge and Tramway Ridge, as these were warm
486 ground areas, exposed to the surface. However, they have very distinct isotope ratios: Tramway Ridge has the
487 one of the lightest of any site (-4.99 ‰), whereas Ice Tower Ridge has a much heavier signature (-1.92 ‰),
488 despite similar exposure to the wind, surface temperatures and sampling methods at both sites. At Hut Cave,
489 sample probes inserted at different depths at the same vent next to one another, and at a second site where
490 gas was blown rapidly out of a crack, yielded very similar δ¹³C values after 1-2 days of pumping, suggesting
491 there were no large kinetic effects at shallow depths for that site. We also observe similarities between δ¹³C
492 measured at different vents within other caves (e.g. Warren, Sauna), despite different rates of gas emission,
493 differing amounts of soil, and different soil temperatures. This does not rule out the possibility of
494 fractionation due to diffuse degassing, and by contrast we do see some variation in δ¹³C at Periscope.
495 However, the overall consistency between vents within each sampling site suggests that factors other than
496 kinetic fractionation have a greater role in determining δ¹³C.

497 (iii) The shallow plumbing at Erebus may be complex on small spatial scales, as evidenced by the
498 variability of plume gas compositions from its lava lakes (Oppenheimer and Kyle, 2008) and
499 changes to summit degassing sites over short time periods. Subsurface magmatic and
500 hydrothermal features could be a factor in the spatial variability of carbon isotope ratios from
501 flank sites. Dissolution of CO₂ in a shallow hydrothermal system and fractionation between
502 dissolved, gaseous, and any precipitating phases (Mook et al., 1974) can cause fractionation.
503 Dissolution in a low temperature hydrothermal system favours lighter values in the gas. This
504 requires temperatures <120°C for HCO₃⁻(aq) – CO₂ (g) equilibrium fractionation, or <192°C in
505 the calcite – CO₂ (g) system (Bottinga, 1968; Zhang et al., 1995; Szaran, 1997; Myrntinen et al.,
506 2012). By contrast, dissolution of a light CO₂ end-member in higher temperature systems (i.e.
507 >120°C in equilibrium with aqueous HCO₃⁻, or >192°C with calcite) could cause fractionation to
508 heavier values.

509 The highest outlet temperatures (59°C) were observed at both Tramway and ITR warm ground sites,
510 which bracket the measured range of carbon isotope ratios. The difference between the two could be
511 explained by the presence (ITR) or absence (Tramway) of a high temperature hydrothermal system. If we
512 assume fractionation solely between dissolved bicarbonate – gaseous CO₂ and take Tramway to represent
513 the unmodified magmatic and most mantle-like gas, fractionation factors suggest a temperature of about
514 200°C could give a +4‰ heavier δ¹³C-CO₂ (Myrntinen et al., 2012), accounting for maximum projected
515 difference measured at ITR compared to Tramway. Lower temperature systems would experience less
516 fractionation, explaining the intermediate values observed at Hut and Periscope caves. Carbon dioxide
517 dissolves more readily into aqueous solutions at low temperatures (Lowenstern, 2001), so that lower
518 fluxes are also expected above low temperature hydrothermal systems. This may account for small
519 difference in fluxes between Tramway and ITR, and high CO₂ concentrations in bag samples at Tramway
520 compared to ITR or the caves. Samples from the crater rim also have a heavier δ¹³C signature despite
521 CO₂ concentrations being close to air. This could result from removal, through dissolution, of magmatic
522 CO₂, combined with fractionation in a high temperature hydrothermal system similar to what we propose
523 beneath ITR.

524 **Table 5.** Properties of degassing sites potentially correlating with measured carbon isotope ratios, showing
 525 that there is no single link between carbon isotope ratios and temperature, depth, CO₂ concentration, or
 526 seismic tomography data. See text for discussion on how these factors may combine to influence δ¹³C.

Site	Seismic tomography ¹	Max vent temperatures ²	Relative depth ³	Projected δ ¹³ C (‰) ⁴	[CO ₂](%) ⁵
Tramway Ridge warm	LVZ	Hot (59°C)	Surface	-5 to -4	1.3-1.8
Ice Tower Ridge warm	HVZ	Hot (59.5°C)	Surface	-1	0.11-0.32
Sauna Cave	LVZ	Hot (43.5°C)	Deep	-4	0.63-1.3
Cathedral Cave	LVZ?	Cool (15°C)	Deep	-3.5	0.67-1.3
Warren Cave	HVZ?	Cool (15.5°C)	Deep	-3	0.7-1.6
Hut Cave	HVZ	Cool (9.7°C)	Shallow	-2	0.24-0.25
Periscope Cave	LVZ	Warm (21°C)	Surface	-2 to -1	0.22-0.34

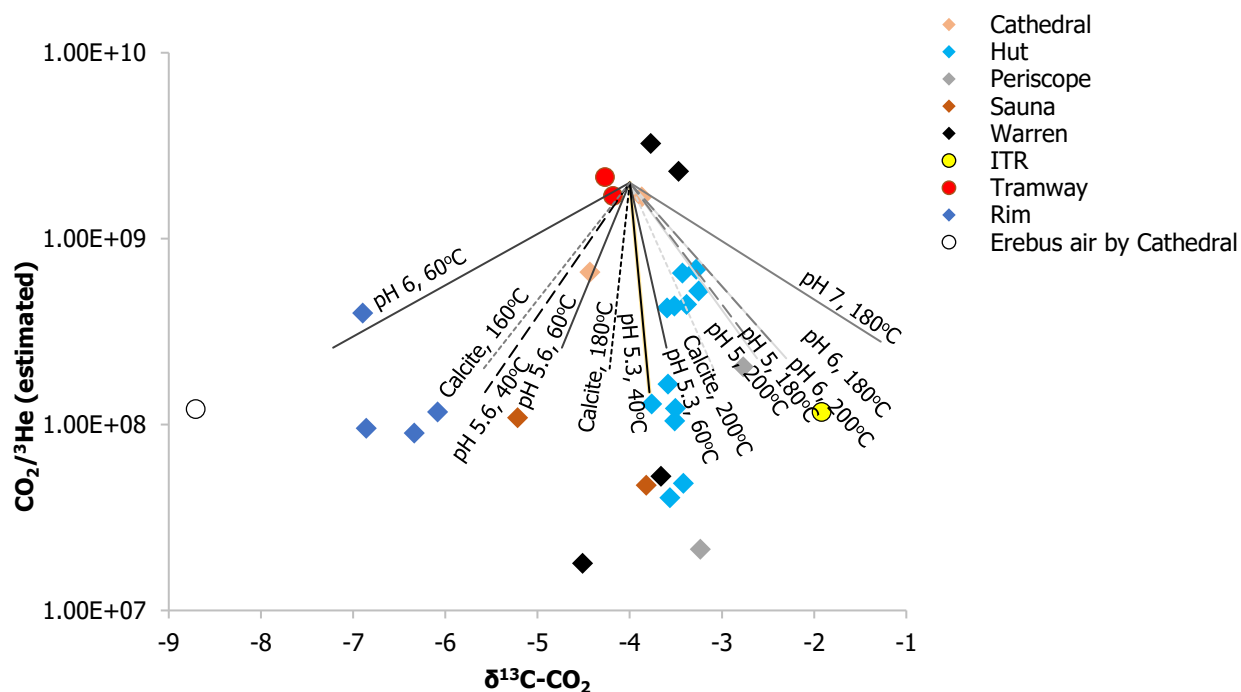
527 ¹From Zandomeneghi et al. 2013. ²Hottest vent temperatures at sample sites in this study. ³Relative to local ground surface. Periscope
 528 cave is largely horizontal, while the vents in Hut Cave are below ground surface (approx. 2-4 m). Warren, Cathedral-Mammoth, and
 529 Sauna, all have entrances over 10 m below the surface ice. ⁴See Figure 4 for projected mixing lines. ⁵Concentrations for Warren,
 530 Tramway, and Sauna are estimates; those for Cathedral were measured directly by Delta Ray before dilution. Hut, Periscope, and ITR
 531 concentrations could be measured directly during the Delta Ray analyses.

532
 533 The source of hydrothermal water is likely meteoric, but the depth at which the interaction with magmatic gas
 534 begins is unknown. The water source is important in considering whether it is plausible that the CO₂
 535 emissions at Periscope (-2 to -1 ‰) could be affected by hydrothermal interactions without any similar effects
 536 nearby at Tramway (-5 to -4 ‰). Localised melting is observed within caves, and refreezing results in the
 537 increased ice density measured by Curtis (2015). Periscope and Hut caves, where surface snow is frequently
 538 blown in to the caves, have heavier projected δ¹³C (-2 to -1 ‰) than the deeper Sauna, Warren, and Cathedral
 539 caves. This might suggest that gases emitted from shallow caves are more influenced by shallow percolation
 540 of meltwater and isotopic fractionation due to dissolution, but only if meltwater could reach sufficiently high
 541 temperatures to cause fractionation to heavier δ¹³C. We do not have enough evidence to determine whether
 542 ice thickness or proximity to the base of the snowpack might influence degassing. In addition to melting in
 543 the summit area, if a larger subglacial groundwater system (Flowers, 2015) were to exist beneath the lower
 544 glaciated flanks of Erebus, there could be a more extensive hydrothermal system circulating to greater depths.
 545

546 For Rayleigh fractionation of CO₂ dissolving in water, with partitioning between CO₂ (g) and calcite or
 547 HCO₃⁻ (aq), using fractionation factors from the literature (Malinin et al., 1967; Clark and Fritz, 1997), we can
 548 consider the range of concentrations and δ¹³C-CO₂ that could be generated by fractionation in a
 549 hydrothermal system. Using CO₂ amounts from GC-QMS analyses, and assuming a helium content of 5.4
 550 ppm (consistent with air) and constant R/R_a, of 1.18, which is the highest measured from our samples, we
 551 follow Gilfillan et al. (2009) to plot estimated CO₂/³He vs δ¹³C (Fig. 10). We see in Figure 10 that direction of
 552 fractionation is influenced both by temperature and pH, with fractionation to heavier carbon isotope ratios in
 553 the discharging CO₂ requiring high temperatures or lower pH. With calcite precipitation, still higher
 554 temperatures are required, as the crossover point when δ¹³C-CO₂ begins fractionating to heavier values is at
 555 around 192°C (Malinin et al., 1967). We note that the assumption of airlike helium content may give
 556 artificially higher CO₂/³He ratios in our samples. However, due to the variation in CO₂ content we consider
 557 the range of carbon isotope ratios that can be generated with slight variations in temperature or pH

558 conditions to support hydrothermal fractionation at Erebus. The mechanism for CO₂ loss and the water pH
559 would be required to constrain the temperature. Regardless of these, however, CO₂ loss of over 99% of the
560 original gas is required to reach the measured amounts. The most likely scenario, therefore, is dilution and
561 removal of CO₂, through air mixing combined with dissolution in a high temperature or slightly acidic
562 hydrothermal system.

563



564

565 **Figure 10.** Possible fractionation pathways from partitioning of CO₂ (g) in water with precipitated calcite or
566 aqueous HCO₃⁻ and H₂CO₃, which is pH dependent. CO₂/³He ratios are from GC-QMS measurements of
567 CO₂, assumed total He of 5.4 ppm, with ³He estimated from a constant R/Ra, assumed to be 1.18, from
568 IRMS analyses of 2012 copper tube samples. The fractionation lines start from CO₂/³He of 2x10⁹, which are
569 likely values for DMM and MORB (Resing et al., 2004; Barry et al., 2014) as well as close to the lower values
570 found by Barfod et al. (1999) for gases from the Cameroon volcanic line. They are calculated up to a
571 dissolved CO₂ fraction of 93% or precipitated calcite of 90%. There is clearly no single fractionation trend
572 that encompasses the range of measured data, and while samples from Hut Cave seem to roughly follow one
573 fractionation trend this is less apparent for other sites such as Warren Cave, potentially reflecting other
574 influences such as multiple stages of interaction with water, and mixing with air or additional magmatic gas.

575

576 4.1.2 Oxygen isotope ratios

577 Attempts to calculate the original oxygen isotope ratios of any water in equilibrium with the measured CO₂,
578 following Chiodini et al. (2000) are prevented by the lack of constraints on equilibration temperatures and
579 H₂O/CO₂ ratios. Sample temperatures are relatively low, and equilibrium is likely to be with liquid water
580 where it is present. The more dilute samples from the crater rim resemble air, which is consistent with the
581 rapid kinetics of ¹⁸O equilibration between CO₂ and H₂O, whereas the lightest oxygen isotope ratios are at
582 Tramway Ridge and ITR, where steaming ground indicates water emissions. We did not collect snow samples
583 from the same sites for oxygen isotope data, but our warm ground data may be consistent with CO₂ re-

584 equilibration to Erebus snowmelt with light $\delta^{18}\text{O}$ due to the altitude (Assonov et al., 2005). The cave samples
585 and cave air fall in an intermediate region, likely indicating a combination of meltwater and air contamination,
586 rather than a heavier magmatic water component. The higher temperature fumaroles in the main crater, and
587 the concentrated plume closer to the lava lake, could not be accessed, but in theory could provide more
588 reliable constraints on oxygen isotopes in combination with $\delta^{18}\text{O}$ - H_2O from snow (e.g. Curtis, 2015).

589

590 **4.1.3 CO₂ flux and concentration**

591 Direct flux measurements at Side Crater, Ice Tower Ridge, and Tramway range from around 120 – 290 $\text{g}\cdot\text{m}^{-2}\cdot\text{d}^{-1}$
592 with a total of about 8.2 $\text{t}\cdot\text{d}^{-1}$. This is lower than the flux estimated for total flank degassing by Wardell et
593 al. (2003), who quantified fluxes out of openings on ice towers and caves as well as warm ground, and found
594 higher fluxes overall, totalling 40 $\text{t}\cdot\text{d}^{-1}$. Their method was based on fewer measurements over a greater area
595 and it is likely that our measurements did not cover the same areas. We included Side Crater, which was not
596 in their study, whereas they report higher fluxes on upper Tramway Ridge (4760 $\text{g}\cdot\text{m}^{-2}\cdot\text{d}^{-1}$), suggesting that our
597 coverage of Tramway was different or that fluxes have changed. Soil degassing at the ITR site appears
598 consistent between our measurements in 2015 and 2016, suggesting stability over these time periods. The
599 CO₂ concentrations from GC-QMS analyses do not exceed 2.9%, which is consistent with amounts measured
600 by Wardell et al. (2003).

601

602 If we assume that the difference in CO₂ fluxes between Tramway and ITR is due to a 200°C hydrothermal
603 system beneath ITR dissolving CO₂ as bicarbonate, we can use the solubility of CO₂ in water to calculate that
604 the approx. 44 $\text{g}\cdot\text{m}^{-2}\cdot\text{d}^{-1}$ that is lost must be interacting with a 6.5×10^6 L volume of water per day. Given our
605 estimates of the surface area at ITR (9164 m^2), this could suggest an aquifer thickness of 2 – 14 m depending
606 on capacities of 5 – 33% water for the aquifer.

607

608 Our attempts to quantify diffuse CO₂ flux in caves were complicated by high CO₂ content in the cave air,
609 which often prevented accurate flushing of the accumulation chamber. In these cases, cave air CO₂ exceeded
610 that measured in samples from the ground. Constant high gas flow may be responsible for more established
611 deep caves at Warren and Cathedral.

612

613 Our flux measurements fall into two broad populations (Fig. 9), the reason for which is not clear.
614 Hydrothermal dissolution of CO₂ cannot account for the CO₂ flux population distributions, as Tramway and
615 ITR have similar distributions, although they have different overall fluxes and carbon isotope ratios that are
616 consistently different. In addition, although CO₂ solubility in water decreases with temperature, ITR has
617 similar or lower concentrations of CO₂ in the sampled gases compared to Hut and Periscope, despite a
618 projected higher temperature hydrothermal system based on its heavier carbon isotope ratios. Combined with
619 the observation that low CO₂ concentration samples have more air-like carbon isotope ratios, this makes it
620 more likely that the degree of air contamination is responsible for the observed CO₂ flux distribution, i.e.
621 lower fluxes could be associated with a higher proportion of atmosphere-derived air.

622

623 **4.2 Gas compositions and atmospheric air**

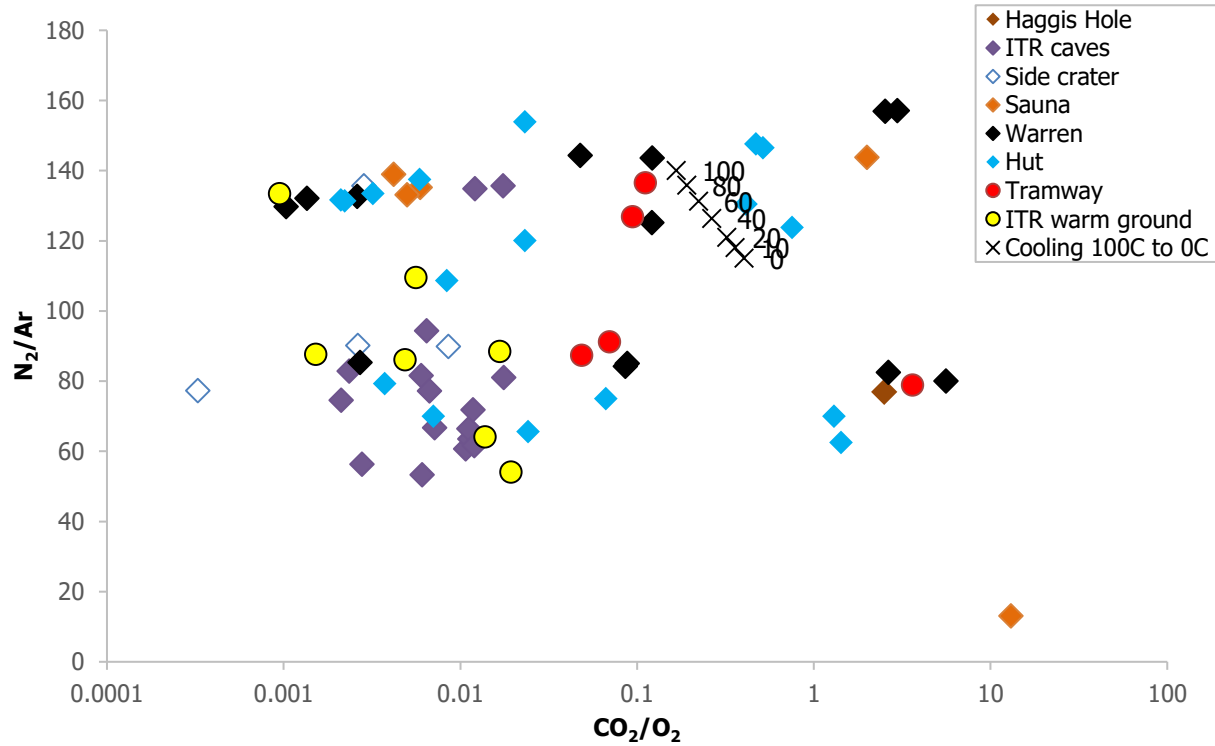
624 Most copper tube and Giggenbach bottle samples are dominated by air (Fig. 3, Table 1). This could be due to
625 contamination during sampling, mixing with cave air before sample collection, recirculation of air through the
626 volcanic edifice (e.g. Bergfeld et al., 2015), or incorporation of air into the convecting lava lake at the summit
627 followed by transport from the degassing magma to the ice caves.

628 If gas flow out of vents is unsteady, pumped samples may contain cave air mixed with occasional pulses of
629 more deeply-sourced gas, which could explain why copper tube sample compositions are variable. This
630 variability may not be picked up over the area and timescales of the flux meter measurements or in collecting
631 1 L of sample for carbon isotope measurements. The nitrogen-rich samples could then represent either a
632 magmatic end-member, or an air-contaminated CO₂ rich gas with oxygen removed (Fig. 3a). Airflow
633 resonance in caves is a recognized phenomenon (Cigna, 1968) that may result in high frequency periodicities
634 in CO₂ concentrations (Faimon et al., 2012). Such observations have focused on cave air and air at cave
635 entrances, but we speculate that similar processes on a smaller scale may affect compositions between
636 duplicate copper tubes at cave vents.

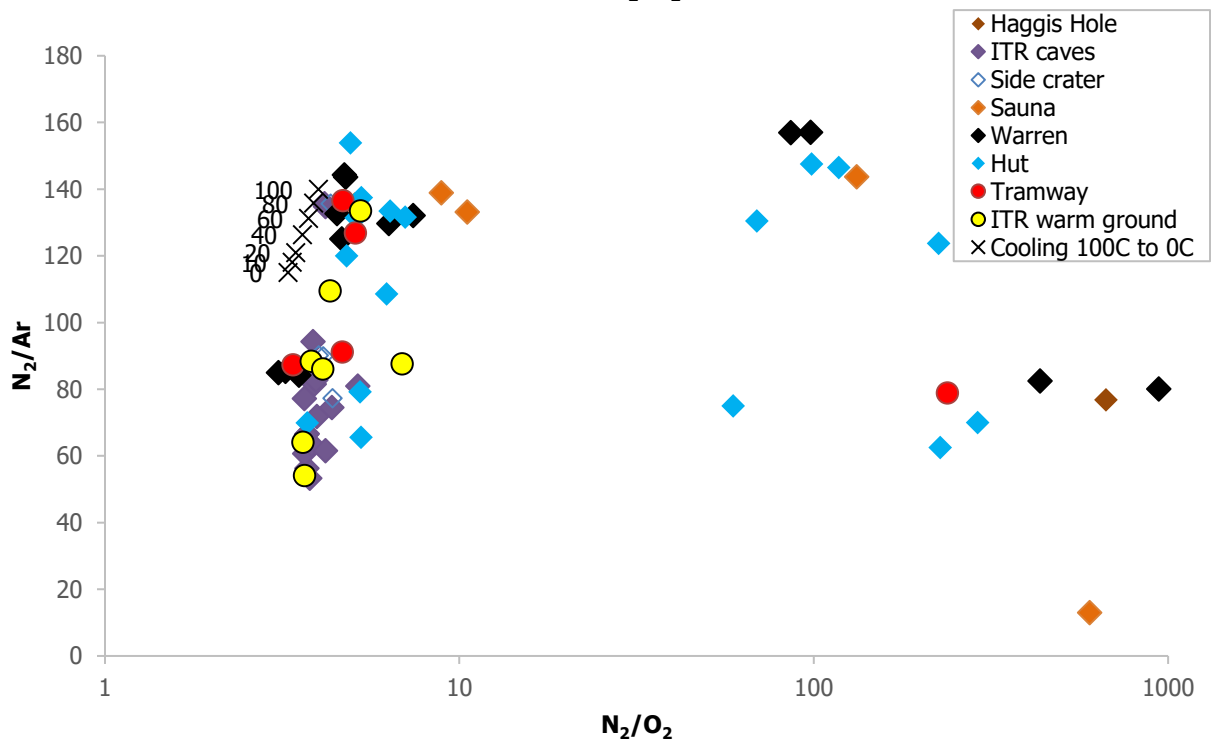
637 Air contributions to vent degassing could also result from more systematic incorporation of atmospheric air
638 via caves or permeable volcanic rock and soil. Mechanisms for this could include differential air temperature
639 or pressure, or wind -driven mixing. Barometric pumping occurs at Warren Cave, and seems to only affect
640 the degree to which air is pulled out of ice towers and caves (Curtis and Kyle, 2011). However, there are other
641 drivers of circulation that have been identified both in caves and on mountain slopes: the temperature-driven
642 chimney effect, with cold air pulled in at lower entrances and warm air emitted at higher ones, and ‘mountain
643 breathing’ caused by wind (Woodcock, 1987). These can occur in porous soils even in the absence of caves or
644 volcanic degassing (Thorstenson et al., 1998; Bergfeld et al., 2015). At Erebus, fractures in the ice cover on
645 the lower flanks, for example at glacial crevasses, and exposed rock or soil in the summit caldera, could
646 permit atmospheric air into the edifice. Emissions of CO₂ in such instances could also be affected by
647 atmospheric conditions and wind-driven circulation (Lewicki et al., 2007; Ogretim et al., 2013). The lava lake
648 is open to the atmosphere and is another potential site for mixing; however, entrainment of cold air at lower
649 levels, rather than at the summit where hot gas is also emitted, is more consistent with the chimney effect.

650 The N₂/Ar and O₂/Ar ratios of gas samples tend to be within the ranges measured for air samples. The
651 N₂/O₂ concentrations, however, range from air-like to having O₂ below detection. In N₂-Ar-O₂ space the N₂-
652 O₂ and Ar-O₂ variations are linear, implying that the nitrogen-rich gas results from oxygen being removed
653 without affecting the N₂/Ar ratios, rather than from magmatic gas containing excess nitrogen mixing with air
654 (Fig. 3c).

655
656 An additional mechanism for modifying air or magmatic gas is dissolution in hydrothermal waters, which is
657 likely to have affected carbon isotope ratios through dissolution of CO₂. Similar fractionation can occur
658 between gases. The solubility of CO₂ in neutral waters is much higher than that of Ar and O₂, which have
659 similar solubilities, while N₂ is less soluble (Sander, 2015). We can calculate the ratios of these species in
660 equilibrium with the exsolved gas at changing temperatures, assuming some initial ratios and temperatures
661 (Fig. 11).



662



663

664 **Figure 11.** Examples of projected gas ratios from dissolution and re-exsolution of gas ($N_2/Ar = 83$, $N_2/O_2 =$

665 4 , $CO_2/O_2 = 1.7$) in water cooling from 100 to $0^\circ C$ (Henry's Law constants from Sander 2015). Labels

666 indicate temperature of the water from which degassing occurs. The range of these ratios produced in this

667 way is smaller than observed in our gas samples, particularly compared to the spread of the x-axis.

668 The difference between measured gas ratios and those of the same species dissolved in pure water is at a

669 maximum at $0^\circ C$. At higher temperatures, this difference decreases, so re-exsolution from cooling water

670 could account, for example, for increasing CO_2/O_2 or decreasing N_2/Ar ratios (Fig. 11). However, the
671 measured range of ratios is far greater than the maximum fractionations indicated by these calculations.
672 Despite the similarity in solubilities between Ar and O_2 , the spread of N_2/O_2 is much greater than that of
673 N_2/Ar and cannot be explained by gas dissolution and re-exsolution. In the following sections we show that
674 oxygen removal, rather than a high nitrogen content, is also supported by $\delta^{15}\text{N}$ and argon isotope data.
675

676 This is also consistent with the relationship between CO_2 and N_2/Ar (Fig. 3b). An initial magmatic gas can be
677 partially stripped of CO_2 in a hydrothermal system. Mixing a small fraction of this gas with air would not
678 noticeably affect N_2/Ar , given that mantle, ASW, and air values for N_2/Ar are relatively close. Oxidation of
679 the surrounding rock could lead to an oxygen depleted air-like composition, potentially retaining some CO_2
680 whose carbon isotope composition reflects hydrothermal interaction. Combustion at the lava lake surface
681 would be a second mechanism to remove oxygen, where magmatic gas could mix with oxygen-depleted air
682 from the surface. However, we suggest that the first scenario is more likely given that pulling such significant
683 proportions of cold air into the lava lake is counter to the chimney effect. We speculate that there is a further
684 possibility of interaction between air and magmatic gases at high temperatures (Martin et al., 2006) but at
685 greater depths in the plumbing system, rather than at the lava lake. Oxidation by reaction between air and
686 magmatic gas rather than rock could also remove CO and H_2 (Giggenbach, 1987), accounting for the low
687 proportion of these species in our samples, though oxidation of CH_4 by oxygen will be slower (Li and
688 Hoflund, 2003). Regardless of the mechanism for oxygen removal, the variability in oxygen content between
689 samples collected in the same time periods also shows that air mixing occurs throughout the system. This
690 could be due to unsteady supply of a magmatic-hydrothermal gas that has been stripped of oxygen, or to
691 variations in the amount of air added subsequently.
692

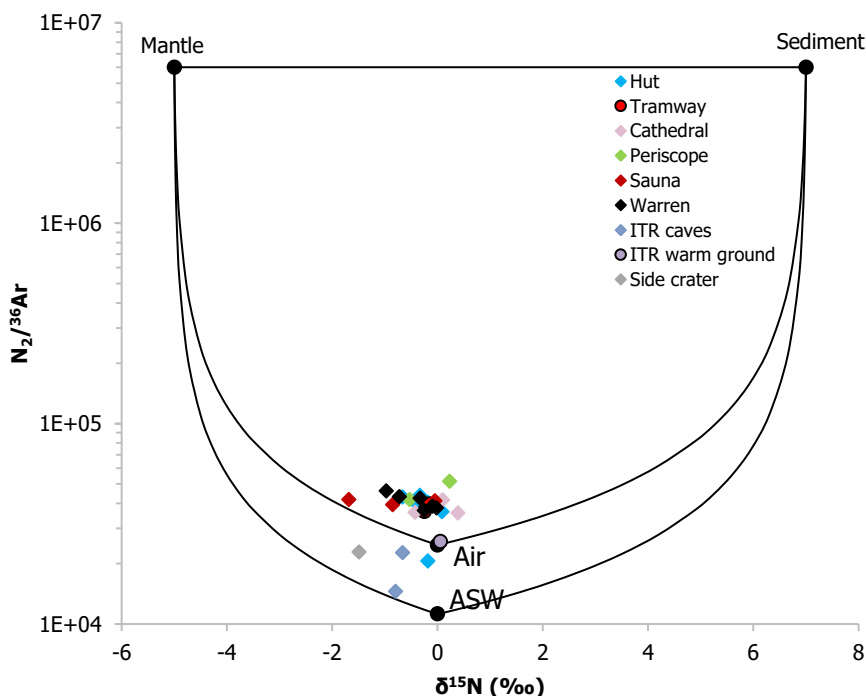
693 Further investigation into helium content and isotope ratios would be valuable in examining these processes.
694 Our limited $^3\text{He}/^4\text{He}$ and $^4\text{He}/^{20}\text{Ne}$ analyses are consistent with air-like compositions. Matched helium
695 content and helium and neon isotope ratios, particularly at sites with higher temperature or higher CO_2
696 content samples such as Warren, Sauna, and Tramway, could be extremely valuable in future work to
697 distinguish between mantle, crustal, and atmospheric gas sources (Gilfillan et al., 2011, 2017).
698

699 4.3 Nitrogen and argon isotopes

700
701 Variations in $\delta^{15}\text{N}$ are small. Most samples are air-like, consistent with N_2/Ar ratios. A range of about -1.5 –
702 0.5‰ suggests a minor contribution from a MORB-type mantle component. Projecting a mixing line between
703 air and the lightest samples towards $\text{O}_2/\text{N}_2 = 0$ gives a nitrogen isotope ratio of about -1.8‰, somewhat
704 heavier than commonly cited MORB mantle values (Marty and Zimmermann, 1999; Mohapatra and Murty,
705 2004). We consider this to be the closest to source values, as kinetic fractionation during open system
706 magmatic degassing is unlikely (Fischer et al., 2005) and would occur alongside fractionation of $\delta^{13}\text{C}-\text{CO}_2$
707 (Cartigny et al., 2001).
708

709 A three-component mixing model (Fig. 12) can be used to examine the likely contributions from mantle, air
710 or air-saturated water (ASW) at 0°C , and sediment sources, following Sano et al. (2001). The $\text{N}_2/^{36}\text{Ar}$ values
711 here are derived from the average $^{40}\text{Ar}/^{36}\text{Ar}$ of 294.07 of our data. This shows that most of our data can be
712 explained by mixing between a mantle end-member and air. As described by Sano et al. (2001), the mixing
713 equations can be used to calculate the contributions of each end-member. Some samples (HUT1, ITR-UWG-
714 11) resemble air despite being emitted at higher than ambient temperatures. The highest potential mantle

715 contribution is from Sauna cave (Sauna-A-2) where 38 % (if mixed with air) to 57% (mixing with ASW) could
 716 be mantle-derived.



717 **Figure 12.** $N_2/^{36}Ar$ vs $\delta^{15}N$ using ^{36}Ar from argon content in each sample and average $^{40}Ar/^{36}Ar$ ratio of all
 718 samples analysed for argon isotopes (294.1), following Sano et al. (2001). While some samples are within the
 719 air to ASW range, others – including those from Warren, Sauna, and Tramway, have higher $N_2/^{36}Ar$ ratios
 720 that could indicate mantle influence.
 721

722 However, an alternative possibility to mixing is that fractionation of nitrogen between gas and dissolution in
 723 water is responsible for the variation in isotope ratios. Experiments by Lee et al. (2015) measured
 724 fractionations from +0.91‰ for N_2 dissolved in water at 5°C to -0.42‰ at 60°C, with a crossover at 40°C.
 725 Regardless of whether fractionation or mixing are responsible for the range of $\delta^{15}N$, the samples from Sauna
 726 Cave with the lightest nitrogen isotope values and highest temperatures are the least modified by atmospheric
 727 air contamination or dissolution and exsolution from the original magmatic gas.
 728

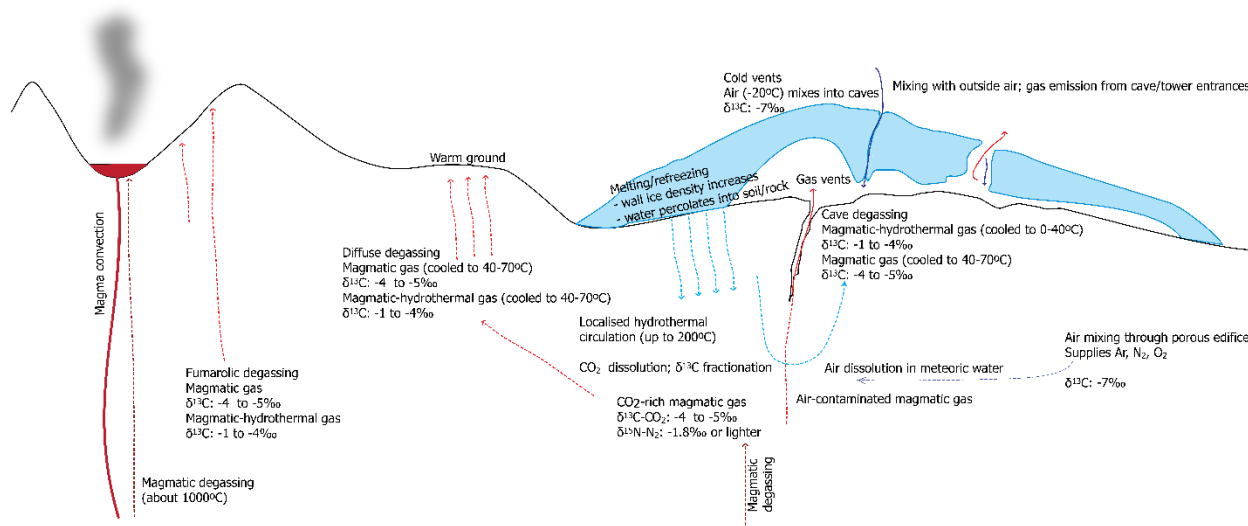
729 Samples from sites other than Sauna Cave, even where N_2/O_2 ratios are high, have more air-like $\delta^{15}N$. This
 730 indicates that the process by which N_2/O_2 is increased is independent of the nitrogen source; oxygen is
 731 removed from gases that are predominantly air as well as from those that contain a greater mantle-derived
 732 component. Argon isotopes are also air-like, with one relatively argon-rich sample (HUT-shallow-14) having a
 733 slightly higher than air (295) $^{40}Ar/^{36}Ar$ of 331.
 734

735 These stable isotope ratios indicate a primarily air-derived gas, which requires a mechanism for removal of
 736 oxygen rather than the addition of nitrogen. As discussed in the previous section, removal of O_2 by
 737 dissolution in water would similarly affect Ar and is inconsistent with observed trends shown in Figures 3 and
 738 11. Another mechanism is a redox reaction with gas or rock that removes oxygen from air. Examples might
 739 be reactions with and removal of reduced gas species such as CO , H_2 , H_2S , and CH_4 . Of these species,
 740 reaction of hydrogen sulfide with iron in rocks may account for sulfur species not being detected in flank
 741

742 degassing (Symonds et al., 2001). The remaining species are only observed in trace amounts in our samples. A
743 more likely scenario is reaction of O₂ with rock close to the surface, resulting in oxidation of the rock and
744 removal of O₂. A final possibility is that microbial oxidation sometimes exceeds the supply of oxygen from
745 atmospheric air. At Warren and neighbouring caves, biological studies have found CO oxidizing bacteria
746 (Tebo et al., 2015), but this cannot account for gas compositions that seem only to have oxygen removed,
747 without increased CO₂. Some combination of these processes may be responsible for oxygen depleted gases.
748

749 4.4 Degassing model and implications

750
751 Figure 13 shows likely pathways contributing to the upper flank degassing of Erebus, with mixing between
752 magmatic and atmospheric gas within the volcano, and interaction between gas and meltwater causing
753 fractionation of elemental gas and carbon and nitrogen isotope ratios. It is likely that melting within void
754 spaces extends from FIC scales to much smaller soil pore scales, with widespread basal melting wherever heat
755 is sufficient. We cannot rule out the possibility that hydrothermal water could be sourced from a larger region
756 extending beneath Erebus' glaciated lower flanks. The presence of a hydrothermal system suggests that
757 previous phreatomagmatic activity may not be solely due to snow cover as previously assumed. Such a system
758 has the potential to dissolve a small proportion of the CO₂ that would otherwise be degassing. While the
759 carbon isotope ratios we measure can be attributed to dissolution of CO₂, the proportions of CO₂ we
760 measured would require a much higher proportion be dissolved. The small difference in CO₂ flux at sites
761 expected to be affected or unaffected by hydrothermal dissolution (about 2 t·d⁻¹ between ITR and Tramway)
762 and the composition of the measured gases indicates that dilution by air is more likely to be responsible for
763 the relatively low proportion of CO₂ (< 3%).



764
765 **Figure 13.** Schematic of upper flank degassing on Erebus (not to scale). The original magmatic signature is
766 modified by air contamination, and in some cases by interaction with a shallow hydrothermal system.
767

768 While degassing from the Erebus summit crater has a partially shallow degassing signature affected by
769 processes occurring within or just below the lake (Oppenheimer et al., 2009; Iacovino, 2015; Ilanko et al.,
770 2015), upper flank degassing should be unaffected by conduit magma flow. Thus, gas measurements taken
771 over time at warm ground or FIC may give some indication as to changes occurring within the shallow
772 magma storage region, or to deeper sources of degassing. Our measurements show variations in small volume
773 copper tube samples that may be due to temporal changes over short time scales. High resolution time series

774 measurements in the field, of both composition and carbon isotope ratios, could be advantageous to
775 understand high frequency variations. Field gas analyses for carbon isotope ratios are possible (Di Martino et
776 al., 2016), but the power requirements and stable conditions currently required for analyses in the field pose a
777 particular challenge on Erebus.

778

779 **5. Conclusions**

780

781 Despite contributing a relatively small proportion of the gas emitted from Erebus, low temperature degassing
782 sites reveal information about the shallow interactions between magmatic gas, meltwater, and atmospheric air
783 in the shallow volcanic edifice. The loss of CO₂ to the hydrothermal system has been estimated and its effects
784 are seen in carbon isotope ratios of CO₂. Magmatic values are around -4‰, with fractionation to heavier
785 values related to dissolution in water. Melting is observed in the warm cave environments and may contribute
786 meteoric water to hydrothermal systems. Water availability varies locally, with potential shallow systems
787 represented by high velocity structures such as that beneath Ice Tower Ridge (Zandomeneghi et al., 2013).
788 While the pre-existing dyke intrusion provides pathways for magmatic gas ascent, there is also a greater
789 degree of interaction with water at high temperatures, resulting in lower fluxes of CO₂, of about two-thirds of
790 that at Tramway Ridge, and fractionation towards heavier carbon isotope ratios closer to -1‰, as the carbon
791 isotopes equilibrate between gaseous CO₂ and other aqueous or precipitating phases, especially HCO₃⁻, and
792 possibly calcite. By contrast, shallow magma bodies at Sauna and Tramway suggested by low seismic velocity
793 regions (Zandomeneghi et al., 2013) are associated with higher CO₂ fluxes and carbon isotope ratios less
794 affected by shallow water or air interaction.

795

796 Samples at many sites contain a high proportion of air, showing that in addition to removal by dissolution,
797 initial concentrations of CO₂ are diluted by air. Although this dilution may be shallow and localized, oxygen
798 depleted samples also contain air-derived nitrogen, indicating that further modification causing oxygen
799 removal must have occurred after air contamination. This suggests that atmospheric air mixes with the
800 magmatic gas more systematically, possibly from wind-driven mountain breathing through the volcanic
801 edifice. Nitrogen isotope ratios show that most samples are heavily influenced by air contamination. Oxygen-
802 poor samples could then result from the removal of air-derived oxygen, though the exact mechanism, for
803 example redox reactions with rocks, or microbial processes, remains unknown.

804

805 The identification and characterization of a liquid-dominated hydrothermal system at Erebus has important
806 implications for availability of liquid water in the subsurface, and the potential for phreatomagmatic
807 eruptions. A warm liquid water phase also provides an additional and previously unrecognized habitat for
808 microorganisms living below the ice and permafrost region of the volcanic edifice.

809

810

811 **Acknowledgements**

812 This material is based upon work supported by the National Science Foundation through the Office of Polar
813 Programs under grants 1443633 (to TF) and 1142083 (to PRK), and through the Division of Earth Sciences
814 under grant 1664246 (to TF). We are grateful to US Antarctic Program personnel, particularly to Lyra Pierotti
815 and Tom Schaefer for assistance in the field, and to Viorel Atudorei and the Centre for Stable Isotopes at
816 UNM for assistance with laboratory analyses. We also thank Marco Liuzzo and an anonymous reviewer for
817 their valuable feedback.

818

819

820 **References**

- 821 Anderson, D.L., 2000. The Statistics and Distribution of Helium in the Mantle. *International Geology Review*
822 42, 289–311. <https://doi.org/10.1080/00206810009465084>
- 823 ASPA No. 175 management plan, 2014. Management Plan for Antarctic Specially Protected Area No. 175.
824 High Altitude Geothermal Sites of the Ross Sea Region (including parts of the summits of Mount
825 Erebus, Ross Island and Mount Melbourne and Mount Rittmann, northern Victoria Land), in:
826 ATCM XXXVII Final Report. Presented at the Antarctic Treaty Consultative Meeting, Brasilia, pp.
827 199-225. https://www.ats.aq/documents/recatt/att553_e.pdf.
- 828 Assonov, S.S., Brenninkmeijer, C.A.M., Jöckel, P., 2005. The 18O isotope exchange rate between firn air CO₂
829 and the firn matrix at three Antarctic sites. *Journal of Geophysical Research: Atmospheres* 110,
830 D18310. <https://doi.org/10.1029/2005JD005769>
- 831 Barfod, D.N., Ballentine, C.J., Halliday, A.N., Fitton, J.G., 1999. Noble gases in the Cameroon line and the
832 He, Ne, and Ar isotopic compositions of high μ (HIMU) mantle. *Journal of Geophysical Research:*
833 *Solid Earth* 104, 29509–29527. <https://doi.org/10.1029/1999JB900280>
- 834 Barry, P.H., Hilton, D.R., Füre, E., Halldórsson, S.A., Grönvold, K., 2014. Carbon isotope and abundance
835 systematics of Icelandic geothermal gases, fluids and subglacial basalts with implications for mantle
836 plume-related CO₂ fluxes. *Geochimica et Cosmochimica Acta* 134, 74–99.
837 <https://doi.org/10.1016/j.gca.2014.02.038>
- 838 Behrendt, J.C., 1999. Crustal and lithospheric structure of the West Antarctic Rift System from geophysical
839 investigations - a review. *Global and Planetary Change* 23, 25–44. [https://doi.org/10.1016/S0921-](https://doi.org/10.1016/S0921-8181(99)00049-1)
840 [8181\(99\)00049-1](https://doi.org/10.1016/S0921-8181(99)00049-1)
- 841 Behrendt, J.C., LeMasurier, W.E., Cooper, A.K., Tessensohn, F., Tréhu, A., Damaske, D., 1991. Geophysical
842 studies of the West Antarctic Rift System. *Tectonics* 10, 1257–1273.
843 <https://doi.org/10.1029/91TC00868>
- 844 Bergfeld, D., Evans, W.C., Howle, J.F., Hunt, A.G., 2015. Magmatic gas emissions at Holocene volcanic
845 features near Mono Lake, California, and their relation to regional magmatism. *Journal of*
846 *Volcanology and Geothermal Research* 292, 70–83.
- 847 Bottinga, Y., 1968. Calculated fractionation factors for carbon and hydrogen isotope exchange in the system
848 carbon dioxide-graphite-methane-hydrogen-water vapor. *Geochimica et Cosmochimica Acta* 33, 49–
849 64.
- 850 Bräuer, K., Geissler, W.H., Kämpf, H., Niedermann, S., Rman, N., 2016. Helium and carbon isotope
851 signatures of gas exhalations in the westernmost part of the Pannonian Basin (SE Austria/NE
852 Slovenia): Evidence for active lithospheric mantle degassing. *Chemical Geology* 422, 60–70.
853 <https://doi.org/10.1016/j.chemgeo.2015.12.016>
- 854 Camarda, M., De Gregorio, S., Favara, R., Gurrieri, S., 2007. Evaluation of carbon isotope fractionation of
855 soil CO₂ under an advective–diffusive regimen: A tool for computing the isotopic composition of
856 unfractionated deep source. *Geochimica et Cosmochimica Acta* 71, 3016–3027.
857 <https://doi.org/10.1016/j.gca.2007.04.002>
- 858 Cartigny, P., 2005. Stable Isotopes and the Origin of Diamond. *Elements* 1, 79–84.
859 <https://doi.org/10.2113/gselements.1.2.79>
- 860 Cartigny, P., Jendrzewski, N., Pineau, F., Petit, E., Javoy, M., 2001. Volatile (C, N, Ar) variability in MORB
861 and the respective roles of mantle source heterogeneity and degassing: the case of the Southwest
862 Indian Ridge. *Earth and Planetary Science Letters* 194, 241–257.
- 863 Chiodini, G., Allard, P., Caliro, S., Parello, F., 2000. ¹⁸O exchange between steam and carbon dioxide in
864 volcanic and hydrothermal gases: implications for the source of water. *Geochimica et Cosmochimica*
865 *Acta* 64, 2479–2488. [https://doi.org/10.1016/S0016-7037\(99\)00445-7](https://doi.org/10.1016/S0016-7037(99)00445-7)
- 866 Chiodini, G., Cioni, R., Guidi, M., Raco, B., Marini, L., 1998. Soil CO₂ flux measurements in volcanic and
867 geothermal areas. *Applied Geochemistry* 13, 543–552. [https://doi.org/10.1016/S0883-](https://doi.org/10.1016/S0883-2927(97)00076-0)
868 [2927\(97\)00076-0](https://doi.org/10.1016/S0883-2927(97)00076-0)

- 869 Christoffersen, P., Bougamont, M., Carter, S.P., Fricker, H.A., Tulaczyk, S., 2014. Significant groundwater
870 contribution to Antarctic ice streams hydrologic budget. *Geophysical Research Letters* 41, 2003–
871 2010. <https://doi.org/10.1002/2014GL059250>
- 872 Cigna, A.A., 1968. An analytical study of air circulation in caves. *International Journal of Speleology* 3, 41–54.
873 <https://doi.org/10.5038/1827-806X.3.1.3>
- 874 Clark, I.D., Fritz, P., 1997. *Environmental Isotopes in Hydrogeology*. CRC Press, Boca Raton, FL.
- 875 Correale, A., Paonita, A., Rizzo, A.L., Grassa, F., Martelli, M., 2015. The carbon-isotope signature of
876 ultramafic xenoliths from the Hyblean Plateau (southeast Sicily, Italy): Evidence of mantle
877 heterogeneity. *Geochemistry, Geophysics, Geosystems* 16, 600–611.
878 <https://doi.org/10.1002/2014GC005656>
- 879 Correale, A., Pelorosso, B., Rizzo, A.L., Coltorti, M., Italiano, F., Bonadiman, C., 2017. A geochemical study
880 of lithospheric mantle beneath Northern Victoria Land (Antarctica): main evidences from volatile
881 content in ultramafic xenoliths, in: *Geophysical Research Abstracts*. Presented at the EGU General
882 Assembly, European Geosciences Union, Vienna, pp. EGU2017-17484.
- 883 Curtis, A., 2015. Dynamics and global relevance of fumarolic ice caves on Erebus Volcano, Antarctica
884 (Ph.D). New Mexico Institute of Mining and Technology, Socorro.
- 885 Curtis, A., Kyle, P.R., 2017. Methods for mapping and monitoring global glaciovolcanism. *Journal of*
886 *Volcanology and Geothermal Research* 333–334, 134–144.
887 <https://doi.org/10.1016/j.jvolgeores.2017.01.017>
- 888 Curtis, A., Kyle, P.R., 2011. Geothermal point sources identified in a fumarolic ice cave on Erebus volcano,
889 Antarctica using fiber optic distributed temperature sensing. *Geophysical Research Letters* 38.
890 <https://doi.org/10.1029/2011GL0482>
- 891 Curtis, A., Kyle, P.R., 2010. Erebus caves database. <https://doi.org/10.15784/600381>
- 892 D’Alessandro, W., Giammanco, S., Parelo, F., 1997. CO₂ output and δ¹³C(CO₂) from Mount Etna as
893 indicators of degassing of shallow asthenosphere. *Bulletin of Volcanology* 58, 455–458.
- 894 de Moor, J.M., Fischer, T.P., Sharp, Z.D., Hilton, D.R., Barry, P.H., Mangasini, F., Ramirez, C., 2013. Gas
895 chemistry and nitrogen isotope compositions of cold mantle gases from Rungwe Volcanic Province,
896 southern Tanzania. *Chemical Geology, Frontiers in Gas Geochemistry* 339, 30–42.
897 <https://doi.org/10.1016/j.chemgeo.2012.08.004>
- 898 Di Martino, M.R., Capasso, G., Camarda, M., 2016. Spatial domain analysis of carbon dioxide from soils on
899 Vulcano Island: implications for CO₂ output evaluation. *Chemical Geology* 444, 59–70.
900 <https://doi.org/10.1016/j.chemgeo.2016.09.037>
- 901 Dibble, R.R., Kyle, P.R., Skov, M.J., 1994. Volcanic activity and seismicity of Mount Erebus, 1986-1994.
902 *Antarctic Journal of the United States* 29, 11–14.
- 903 Faimon, J., Troppova, D., Baldik, V., Novotny, R., 2012. Air circulation and its impact on microclimatic
904 variables in the Císarska Cave (Moravian Karst, Czech Republic). *International Journal of*
905 *Climatology* 32, 599–623. <https://doi.org/10.1002/joc.2298>
- 906 Federico, C., Corso, P.P., Fiordilino, E., Cardellini, C., Chiodini, G., Parelo, F., Pisciotta, A., 2010.
907 CO₂ degassing at La Solfatara volcano (Phlegrean Fields): Processes affecting δ¹³C and δ¹⁸O of soil
908 CO₂. *Geochimica et Cosmochimica Acta* 74, 3521–3538. <https://doi.org/10.1016/j.gca.2010.03.010>
- 909 Fielding, C.R., Browne, G.H., Field, B., Florindo, F., Harwood, D.M., Krissek, L.A., Levy, R.H., Panter, K.S.,
910 Passchier, S., Pekar, S.F., 2011. Sequence stratigraphy of the ANDRILL AND-2A drillcore,
911 Antarctica: A long-term, ice-proximal record of Early to Mid-Miocene climate, sea-level and glacial
912 dynamism. *Palaeogeography, Palaeoclimatology, Palaeoecology* 305, 337–351.
913 <https://doi.org/10.1016/j.palaeo.2011.03.026>
- 914 Fischer, Takahata, N., Sano, Y., Sumino, H., Hilton, D.R., 2005. Nitrogen isotopes of the mantle: insights
915 from mineral separates. *Geophysical Research Letters* 32, L11305.
916 <https://doi.org/10.1029/2005GL022792>
- 917 Fischer, T.P., Chiodini, G., 2015. Volcanic, Magmatic and Hydrothermal Gases, in: Sigurdsson, H.,
918 Houghton, B., McNutt, S., Rymer, H., Stix, J. (Eds.), *The Encyclopedia of Volcanoes*. pp. 779–797.
- 919 Fischer, T.P., Lopez, T.M., 2016. First airborne samples of a volcanic plume for δ¹³C of CO₂ determinations.
920 *Geophys. Res. Lett.* 43, 2016GL068499. <https://doi.org/10.1002/2016GL068499>

- 921 Flowers, G.E., 2015. Modelling water flow under glaciers and ice sheets. *Proceedings of the Royal Society A:*
 922 *Mathematical, Physical and Engineering Sciences* 471, 20140907–20140907.
 923 <https://doi.org/10.1098/rspa.2014.0907>
- 924 Gerlach, T.M., Taylor, B.E., 1990. Carbon isotope constraints on degassing of carbon dioxide from Kilauea
 925 Volcano. *Geochimica et Cosmochimica Acta* 54, 2051–2058. [https://doi.org/10.1016/0016-](https://doi.org/10.1016/0016-7037(90)90270-U)
 926 [7037\(90\)90270-U](https://doi.org/10.1016/0016-7037(90)90270-U)
- 927 Giggenbach, W.F., 1987. Redox processes governing the chemistry of fumarolic gas discharges from White
 928 Island. *Applied Geochemistry* 2, 143–161.
- 929 Giggenbach, W.F., 1975. A simple method for the collection and analysis of volcanic gas samples. *Bull*
 930 *Volcanol* 39, 132–145. <https://doi.org/10.1007/BF02596953>
- 931 Gilfillan, S.M.V., Lollar, B.S., Holland, G., Blagburn, D., Stevens, S., Schoell, M., Cassidy, M., Ding, Z., Zhou,
 932 Z., Lacrampe-Couloume, G., Ballentine, C.J., 2009. Solubility trapping in formation water as
 933 dominant CO₂ sink in natural gas fields. *Nature* 458, 614–618. <https://doi.org/10.1038/nature07852>
- 934 Gilfillan, S.M.V., Sherk, G.W., Poreda, R.J., Haszeldine, R.S., 2017. Using noble gas fingerprints at the Kerr
 935 Farm to assess CO₂ leakage allegations linked to the Weyburn-Midale CO₂ monitoring and storage
 936 project. *International Journal of Greenhouse Gas Control* 63, 215–225.
 937 <https://doi.org/10.1016/j.ijggc.2017.05.015>
- 938 Gilfillan, S.M.V., Wilkinson, M., Haszeldine, R.S., Shipton, Z.K., Nelson, S.T., Poreda, R.J., 2011. He and Ne
 939 as tracers of natural CO₂ migration up a fault from a deep reservoir. *International Journal of*
 940 *Greenhouse Gas Control* 5, 1507–1516. <https://doi.org/10.1016/j.ijggc.2011.08.008>
- 941 Hall, J., Wilson, T., Henrys, S., 2007. Structure of the central Terror Rift, western Ross Sea, Antarctica. A.K.
 942 Cooper., C.R. Raymond et al. (eds). *Antarctica: A Keystone in a Changing World - Online*
 943 *proceedings of the 10th ISAES, USGS Open-File Report 2007-1047 5.*
 944 <https://doi.org/10.3133/of2007-1047.srp108>
- 945 Harpel, C.J., Kyle, P.R., Dunbar, N.W., 2008. Englacial tephrostratigraphy of Erebus volcano, Antarctica.
 946 *Journal of Volcanology and Geothermal Research* 177, 549–568.
 947 <https://doi.org/10.1016/j.jvolgeores.2008.06.001>
- 948 Harry, D.L., Anoka, J.L., Jha, S., 2018. Geodynamic models of the West Antarctic Rift System: Implications
 949 for the mantle thermal state. *Geosphere* 14, 2407–2429. <https://doi.org/10.1130/GES01594.1>
- 950 Henrys, S., Wilson, T., Whittaker, J.M., Fielding, C., Hall, J., Naish, T., 2007. Tectonic history of mid-Miocene
 951 to present southern Victoria Land Basin, inferred from seismic stratigraphy in McMurdo Sound,
 952 Antarctica. A.K. Cooper., C.R. Raymond et al. (eds). *Antarctica: A Keystone in a Changing World -*
 953 *Online proceedings of the 10th ISAES, Open-File Report USGS Open-File Report 2007-1047, 4.*
 954 <https://doi.org/10.3133/of2007-1047.srp049>
- 955 Huybers, P., Langmuir, C., 2009. Feedback between deglaciation, volcanism, and atmospheric CO₂. *Earth and*
 956 *Planetary Science Letters* 286, 479–491. <https://doi.org/10.1016/j.epsl.2009.07.014>
- 957 Iacovino, K., 2015. Linking subsurface to surface degassing at active volcanoes: A thermodynamic model
 958 with applications to Erebus volcano. *Earth and Planetary Science Letters* 431, 59–74.
 959 <https://doi.org/10.1016/j.epsl.2015.09.016>
- 960 Ilanko, T., Oppenheimer, C., Burgisser, A., Kyle, P.R., 2015. Cyclic degassing of Erebus volcano, Antarctica.
 961 *Bulletin of Volcanology* 77. <https://doi.org/10.1007/s00445-015-0941-z>
- 962 Iverson, N.A., Kyle, P.R., Dunbar, N.W., McIntosh, W.C., Pearce, N.J.G., 2014. Eruptive history and
 963 magmatic stability of Erebus volcano, Antarctica: insights from englacial tephra. *Geochemistry,*
 964 *Geophysics, Geosystems* 15, 4180–4202. <https://doi.org/10.1002/2014GC005435>
- 965 Iverson, N.A., Lieb-Lappen, R., Dunbar, N.W., Obbard, R., Kim, E., Golden, E., 2017. The first physical
 966 evidence of subglacial volcanism under the West Antarctic Ice Sheet. *Scientific Reports* 7, 11457.
 967 <https://doi.org/10.1038/s41598-017-11515-3>
- 968 Javoy, M., Pineau, F., Delorme, H., 1986. Carbon and nitrogen isotopes in the mantle. *Chemical Geology,*
 969 *Isotopes in Geology—Picciotto Volume* 57, 41–62. [https://doi.org/10.1016/0009-2541\(86\)90093-8](https://doi.org/10.1016/0009-2541(86)90093-8)
- 970 Javoy, M., Pineau, F., Iiyama, I., 1978. Experimental determination of the isotopic fractionation between
 971 gaseous CO₂ and carbon dissolved in tholeiitic magma. *Contributions to Mineralogy and Petrology*
 972 67, 35–39.

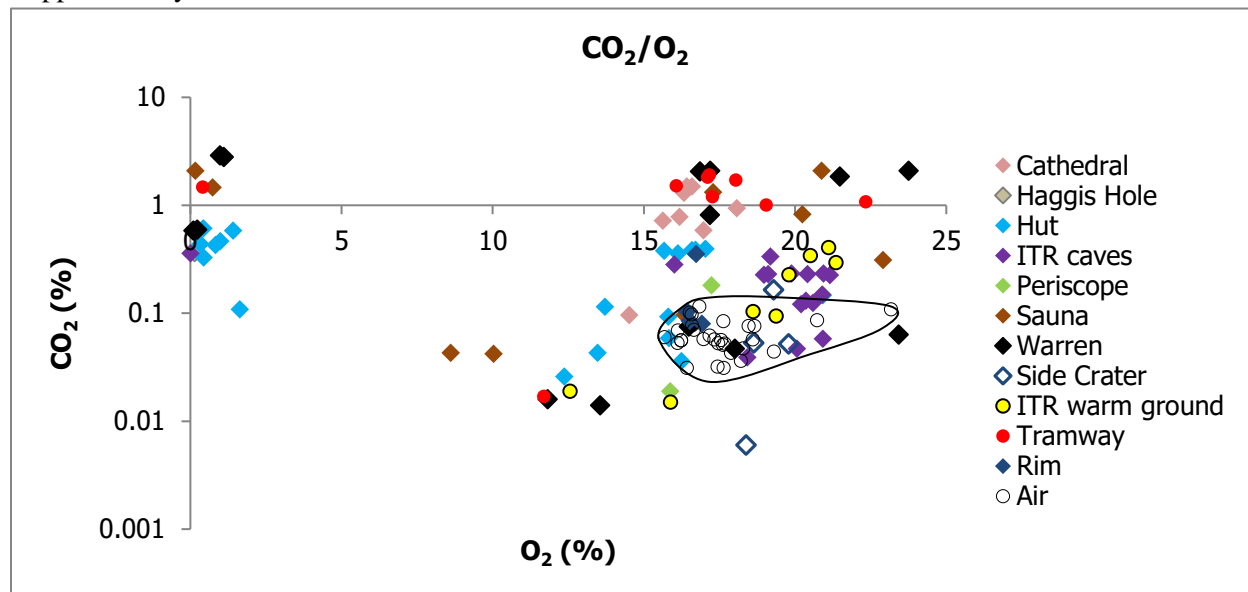
- 973 Kyle, P.R., Moore, J.A., Thirwall, M.F., 1992. Petrologic Evolution of Anorthoclase Phonolite Lavas at
 974 Mount Erebus, Ross Island, Antarctica. *Journal of Petrology* 33, 849–875.
 975 <https://doi.org/10.1093/petrology/33.4.849>
- 976 Lee, H., Fischer, T.P., de Moor, J.M., Sharp, Z.D., Takahata, N., Sano, Y., 2017. Nitrogen recycling at the
 977 Costa Rican subduction zone: The role of incoming plate structure. *Scientific Reports* 7, 13933.
 978 <https://doi.org/10.1038/s41598-017-14287-y>
- 979 Lee, H., Muirhead, J.D., Fischer, T.P., Ebinger, C.J., Kattenhorn, S.A., Sharp, Z.D., Kianji, G., 2016. Massive
 980 and prolonged deep carbon emissions associated with continental rifting. *Nature Geoscience* 9, 145–
 981 149. <https://doi.org/10.1038/ngeo2622>
- 982 Lee, H., Sharp, Z.D., Fischer, Tobias P., 2015. Kinetic nitrogen isotope fractionation between air and
 983 dissolved N₂ in water: Implications for hydrothermal systems. *Geochemical Journal* 49, 571–573.
 984 <https://doi.org/10.2343/geochemj.2.0380>
- 985 LeMasurier, W.E., 2008. Neogene extension and basin deepening in the West Antarctic rift inferred from
 986 comparisons with the East African rift and other analogs. *Geology* 36, 247–250.
 987 <https://doi.org/10.1130/G24363A.1>
- 988 LeMasurier, W.E., 1990. Late Cenozoic volcanism on the Antarctic Plate: An overview, in: LeMasurier, W.E.,
 989 Thomson, J.W., Baker, P.E., Kyle, P.R., Rowley, P.D., Smellie, J.L., Verwoerd, W.J. (Eds.), *Antarctic*
 990 *Research Series*. American Geophysical Union, Washington, D. C., pp. 1–17.
 991 <https://doi.org/10.1029/AR048p0001>
- 992 Lewicki, J.L., Hillel, G.E., Tosha, T., Aoyagi, R., Yamamoto, K., Benson, S.M., 2007. Dynamic coupling of
 993 volcanic CO₂ flow and wind at the Horseshoe Lake tree kill, Mammoth Mountain, California.
 994 *Geophysical Research Letters* 34. <https://doi.org/10.1029/2006GL028848>
- 995 Li, Z., Hoflund, G.B., 2003. A review on complete oxidation of methane at low temperatures. *Journal of*
 996 *Natural Gas Chemistry* 12, 154–160.
- 997 Lough, A.C., Wiens, D.A., Barcheck, C.G., Anandakrishnan, S., Aster, R.C., Blankenship, D.D., Huerta, A.D.,
 998 Nyblade, A., Young, D.A., Wilson, T.J., 2013. Seismic detection of an active subglacial magmatic
 999 complex in Marie Byrd Land, Antarctica. *Nature Geoscience* 6, 1031–1035.
 1000 <https://doi.org/doi:10.1038/ngeo1992>
- 1001 Lowenstern, J.B., 2001. Carbon dioxide in magmas and implications for hydrothermal systems. *Mineralium*
 1002 *Deposita* 36, 490–502. <https://doi.org/10.1007/s001260100185>
- 1003 Lyon, G.L., Giggenbach, W.F., 1974. Geothermal activity in Victoria Land, Antarctica. *New Zealand Journal*
 1004 *of Geology and Geophysics* 17, 511–521. <https://doi.org/10.1080/00288306.1973.10421578>
- 1005 Malinin, S.D., Kropotova, O.I., Grinenko, V.A., Vernadskiy, V.I., 1967. Experimental determination of
 1006 equilibrium constants for carbon isotope exchange in the system CO₂ (g)-HCO₃ (sol) under
 1007 hydrothermal conditions. *Geochemistry International* 4, 764–771.
- 1008 Martin, A.P., Cooper, A.F., Price, R.C., 2014. Increased mantle heat flow with on-going rifting of the West
 1009 Antarctic rift system inferred from characterisation of plagioclase peridotite in the shallow Antarctic
 1010 mantle. *Lithos* 190–191, 173–190. <https://doi.org/10.1016/j.lithos.2013.12.012>
- 1011 Martin, R.S., Mather, T.A., Pyle, D.M., 2006. High-temperature mixtures of magmatic and atmospheric gases.
 1012 *Geochemistry, Geophysics, Geosystems* 7. <https://doi.org/10.1029/2005GC001186>
- 1013 Marty, B., Zimmermann, L., 1999. Volatiles (He, C, N, Ar) in mid-ocean ridge basalts: Assessment of
 1014 shallow-level fractionation and characterization of source composition. *Geochimica et*
 1015 *Cosmochimica Acta* 63, 3619–3633.
- 1016 Matthey, D.P., 1991. Carbon dioxide solubility and carbon isotope fractionation in basaltic melt. *Geochimica et*
 1017 *Cosmochimica Acta* 55, 3467–3473. [https://doi.org/10.1016/0016-7037\(91\)90508-3](https://doi.org/10.1016/0016-7037(91)90508-3)
- 1018 Mikucki, J.A., Auken, E., Tulaczyk, S., Virginia, R.A., Schamper, C., Sorenson, K.I., Doran, P.T., Dugan, H.,
 1019 Foley, N., 2015. Deep groundwater and potential subsurface habitats beneath an Antarctic dry valley.
 1020 *Nature Communications* 6, 6831. <https://doi.org/10.1038/ncomms7831>
- 1021 Mohapatra, R.K., Murty, S.V.S., 2004. Nitrogen isotopic composition of the MORB mantle: A reevaluation.
 1022 *Geochemistry, Geophysics, Geosystems* 5, Q01001. <https://doi.org/10.1029/2003GC000612>

- 1023 Mook, W.G., Bommerson, J.C., Staverman, W.H., 1974. Carbon isotope fractionation between dissolved
1024 bicarbonate and gaseous carbon dioxide. *Earth and Planetary Science Letters* 22, 169–176.
1025 [https://doi.org/10.1016/0012-821X\(74\)90078-8](https://doi.org/10.1016/0012-821X(74)90078-8)
- 1026 Myrntinen, A., Becker, V., Barth, J.A.C., 2012. A review of methods used for equilibrium isotope fractionation
1027 investigations between dissolved inorganic carbon and CO₂. *Earth-Science Reviews* 115, 192–199.
1028 <https://doi.org/10.1016/j.earscirev.2012.08.004>
- 1029 Ogretim, E., Crandall, D., Gray, D.D., Bromhal, G.S., 2013. Effects of atmospheric dynamics on CO₂
1030 seepage at Mammoth Mountain, California, USA. *The Journal of Computational Multiphase Flows* 5,
1031 283–294.
- 1032 Oppenheimer, C., Kyle, P.R., 2008. Probing the magma plumbing of Erebus volcano, Antarctica, by open-
1033 path FTIR spectroscopy of gas emissions. *Journal of Volcanology and Geothermal Research* 177,
1034 743–754. <https://doi.org/10.1016/j.jvolgeores.2007.08.022>
- 1035 Oppenheimer, C., Lomakina, A.S., Kyle, P.R., Kingsbury, N.G., Boichu, M., 2009. Pulsatory magma supply to
1036 a phonolite lava lake. *Earth and Planetary Science Letters* 284, 392–398.
1037 <https://doi.org/10.1016/j.epsl.2009.04.043>
- 1038 Oppenheimer, C., Moretti, R., Kyle, P.R., Eschenbacher, A., Lowenstern, J.B., Hervig, R.L., Dunbar, N.W.,
1039 2011. Mantle to surface degassing of alkalic magmas at Erebus volcano, Antarctica. *Earth and*
1040 *Planetary Science Letters* 306, 261–271. <https://doi.org/10.1016/j.epsl.2011.04.005>
- 1041 Panter, K.S., Castillo, P., Krans, S., Deering, C., McIntosh, W., Valley, J.W., Kitajima, K., Kyle, P., Hart, S.,
1042 Blusztajn, J., 2018. Melt Origin across a Rifted Continental Margin: a Case for Subduction-related
1043 Metasomatic Agents in the Lithospheric Source of Alkaline Basalt, NW Ross Sea, Antarctica. *J*
1044 *Petrology* 59, 517–558. <https://doi.org/10.1093/petrology/egy036>
- 1045 Panter, K.S., Winter, B., 2008. Geology of the Side Crater of the Erebus volcano, Antarctica. *Journal of*
1046 *Volcanology and Geothermal Research, Volcanology of Erebus volcano, Antarctica* 177, 578–588.
- 1047 Parmelee, D.E.F., Kyle, P.R., Kurz, M.D., Marrero, S.M., Phillips, F.M., 2015. A new Holocene eruptive
1048 history of Erebus volcano, Antarctica using cosmogenic ³He and ³⁶Cl exposure ages. *Quaternary*
1049 *Geochronology* 30, 114–131. <https://doi.org/10.1016/j.quageo.2015.09.001>
- 1050 Phillips, E.H., Sims, K.W.W., Blichert-Toft, J., Aster, R.C., Gaetani, G.A., Kyle, P.R., Wallace, P.J.,
1051 Rasmussen, D.J., 2018. The nature and evolution of mantle upwelling at Ross Island, Antarctica, with
1052 implications for the source of HIMU lavas. *Earth and Planetary Science Letters* 498, 38–53.
1053 <https://doi.org/10.1016/j.epsl.2018.05.049>
- 1054 Rasmussen, D.J., Kyle, P.R., Wallace, P.J., Sims, K.W.W., Gaetani, G.A., Phillips, E.H., 2017. Understanding
1055 Degassing and Transport of CO₂-rich Alkalic Magmas at Ross Island, Antarctica using Olivine-
1056 Hosted Melt Inclusions. *J Petrology* 58, 841–861. <https://doi.org/10.1093/petrology/egx036>
- 1057 Resing, J.A., Lupton, J.E., Feely, R.A., Lilley, M.D., 2004. CO₂ and ³He in hydrothermal plumes: implications
1058 for mid-ocean ridge CO₂ flux. *Earth and Planetary Science Letters* 226, 449–464.
1059 <https://doi.org/10.1016/j.epsl.2004.07.028>
- 1060 Rilling, S., Mukasa, S., Wilson, T., Lawver, L., Hall, C., 2009. New determinations of ⁴⁰Ar/³⁹Ar isotopic ages
1061 and flow volumes for Cenozoic volcanism in the Terror Rift, Ross Sea, Antarctica - Rilling - 2009 -
1062 *Journal of Geophysical Research: Solid Earth - Wiley Online Library. Journal of Geophysical*
1063 *Research* 114. <https://doi.org/10.1029/2009JB006303>
- 1064 Rocchi, S., Armienti, P., D’Orazio, M., Tonarini, S., Wijbrans, J.R., Vincenzo, G.D., 2002. Cenozoic
1065 magmatism in the western Ross Embayment: Role of mantle plume versus plate dynamics in the
1066 development of the West Antarctic Rift System. *Journal of Geophysical Research: Solid Earth* 107,
1067 ECV 5-1-ECV 5-22. <https://doi.org/10.1029/2001JB000515>
- 1068 Rothman, L.S., Gordon, I.E., Babikov, Y., Barbe, A., Chris Benner, D., Bernath, P.F., Birk, M., Bizzocchi, L.,
1069 Boudon, V., Brown, L.R., Campargue, A., Chance, K., Cohen, E.A., Coudert, L.H., Devi, V.M.,
1070 Drouin, B.J., Fayt, A., Flaud, J.-M., Gamache, R.R., Harrison, J.J., Hartmann, J.M., Hill, C., Hodges,
1071 J.T., Jacquemart, D., Jolly, A., Lamouroux, J., Le Roy, R.J., Li, G., Long, D.A., Lyulin, O.M., Mackie,
1072 C.J., Massie, S.T., Mikhailenko, S.N., Müller, H.S.P., Naumenko, O.V., Nikitin, A.V., Orphal, J.,
1073 Perevalov, V.I., Perrin, A., Polovtseva, E.R., Richard, C., Smith, M.A.H., Starikova, E., Sung, K.,
1074 Tashkun, S.A., Tennyson, J., Toon, G.C., Tyuterev, V.G., Wagner, G., 2013. The HITRAN2012

- 1075 molecular spectroscopic database. *Journal of Quantitative Spectroscopy & Radiative Transfer* 130, 4–
1076 50.
- 1077 Sander, R., 2015. Compilation of Henry's law constants (version 4.0) for water as solvent. *Atmospheric*
1078 *Chemistry and Physics* 15, 4399–4981. <https://doi.org/10.5194/acp-15-4399-2015>
- 1079 Sano, Y., Takahata, N., Nishio, Y., Fischer, T.P., Williams, S.N., 2001. Volcanic flux of nitrogen from the
1080 Earth. *Chemical Geology* 171, 263–271. [https://doi.org/10.1016/S0009-2541\(00\)00252-7](https://doi.org/10.1016/S0009-2541(00)00252-7)
- 1081 Sano, Y., Tokutake, T., Takahata, N., 2008. Accurate Measurement of Atmospheric Helium Isotopes.
1082 *Analytical Sciences* 24, 521–525. <https://doi.org/10.2116/analsci.24.521>
- 1083 Sano, Y., Wakita, H., 1985. Geographical distribution of $^3\text{He}/^4\text{He}$ ratios in Japan: Implications for arc
1084 tectonics and incipient magmatism. *J. Geophys. Res.* 90, 8729–8741.
1085 <https://doi.org/10.1029/JB090iB10p08729>
- 1086 Schipper, C.I., Moussallam, Y., Curtis, A., Peters, N., Barnie, T., Bani, P., Jost, H.J., Hamilton, D., Aiuppa, A.,
1087 Tamburello, G., Giudice, G., 2017. Isotopically ($\delta^{13}\text{C}$ and $\delta^{18}\text{O}$) heavy volcanic plumes from
1088 Central Andean volcanoes: a field study. *Bull Volcanol* 79, 65. <https://doi.org/10.1007/s00445-017-1146-4>
- 1090 Scopelliti, G., Bellanca, A., Neri, R., 2011. Petrography and carbonate isotope stratigraphy from MIS AND-
1091 1B core, Antarctica: Evidence of the early Pliocene warming event. *Global and Planetary Change* 76,
1092 22–32. <https://doi.org/10.1016/j.gloplacha.2010.11.006>
- 1093 Sims, K.W.W., Blichert-Toft, J., Kyle, P.R., Pichat, S., Gauthier, P.-J., Blusztajn, J., Kelly, P., Ball, L., Layne,
1094 G., 2008. A Sr, Nd, Hf, and Pb isotope perspective on the genesis and long-term evolution of
1095 alkaline magmas from Erebus volcano, Antarctica. *Journal of Volcanology and Geothermal Research*
1096 177, 606–618. [https://doi.org/doi:DOI: 10.1016/j.jvolgeores.2007.08.006](https://doi.org/doi:DOI:10.1016/j.jvolgeores.2007.08.006)
- 1097 Symonds, R.B., Gerlach, T.M., Reed, M.H., 2001. Magmatic gas scrubbing: implications for volcano
1098 monitoring. *Journal of Volcanology and Geothermal Research* 108, 303–341.
1099 [https://doi.org/10.1016/S0377-0273\(00\)00292-4](https://doi.org/10.1016/S0377-0273(00)00292-4)
- 1100 Szaran, J., 1997. Achievement of carbon isotope equilibrium in the system HCO_3^- (solution) - CO_2 (gas).
1101 *Chemical Geology* 142, 79–86. [https://doi.org/10.1016/S0009-2541\(97\)00077-6](https://doi.org/10.1016/S0009-2541(97)00077-6)
- 1102 Tebo, B.M., Davis, R.E., Anitori, R.P., Connell, L.B., Schiffman, P., Staudigel, H., 2015. Microbial
1103 communities in dark oligotrophic volcanic ice cave ecosystems of Mt. Erebus, Antarctica. *Frontiers*
1104 *in Microbiology* 6. <https://doi.org/10.3389/fmicb.2015.00179>
- 1105 Thorstenson, D.C., Weeks, E.P., Haas, H., Busenberg, E., Plummer, L.N., Peters, C.A., 1998. Chemistry of
1106 unsaturated zone gases sampled in open boreholes at the crest of Yucca Mountain, Nevada: Data and
1107 basic concepts of chemical and physical processes in the mountain. *Water Resources Research* 34,
1108 1507–1529. <https://doi.org/10.1029/98WR00267>
- 1109 van Wyk de Vries, M., Bingham, R.G., Hein, A.S., 2018. A new volcanic province: an inventory of subglacial
1110 volcanoes in West Antarctica. Geological Society, London, Special Publications 461, 231–248.
1111 <https://doi.org/10.1144/SP461.7>
- 1112 Wardell, L.J., Kyle, P.R., Campbell, A.R., 2003. Carbon dioxide emissions from fumarolic ice towers, Mount
1113 Erebus volcano, Antarctica, in: *Volcanic Degassing*, Special Publication. Geological Society, London,
1114 pp. 231–246.
- 1115 Woodcock, A.H., 1987. Mountain breathing revisited - the hyperventilation of a volcano cinder cone. *Bulletin*
1116 *of the American Meteorological Society* 68, 125–130. [https://doi.org/10.1175/1520-0477\(1987\)068<0125:MBRHOA>2.0.CO;2](https://doi.org/10.1175/1520-0477(1987)068<0125:MBRHOA>2.0.CO;2)
- 1118 Zandomenighi, D., Aster, R., Kyle, P.R., Barclay, A., Chaput, J., Knox, H., 2013. Internal structure of Erebus
1119 volcano, Antarctica imaged by high-resolution active-source seismic tomography and coda
1120 interferometry. *Journal of Geophysical Research: Solid Earth* 118, 1067–1078.
1121 <https://doi.org/10.1002/jgrb.50073>
- 1122 Zhang, J., Quay, P.D., Wilbur, D.O., 1995. Carbon isotope fractionation during gas-water exchange and
1123 dissolution of CO_2 . *Geochimica et Cosmochimica Acta* 59, 107–114.
- 1124 Zimbelman, D.R., Rye, R.O., Landis, G.P., 2000. Fumaroles in ice caves on the summit of Mount Rainier:
1125 preliminary stable isotope, gas, and geochemical studies. *Journal of Volcanology and Geothermal*
1126 *Research* 97, 457–473. [https://doi.org/10.1016/S0377-0273\(99\)00180-8](https://doi.org/10.1016/S0377-0273(99)00180-8)

1127
1128

Supplementary Materials A: CO₂/O₂ ratios



1129

1130 Figure A1: CO₂/O₂ from GC-QMS showing samples with air-like or higher CO₂ can be oxygen depleted.
1131 Samples with intermediate oxygen levels between air and oxygen depleted samples have CO₂ content of
1132 140 - 1100 ppm (the most CO₂ depleted sample is from a Giggenbach bottle in 2015 that has air-like O₂
1133 but about 60 ppm CO₂).

1134 Supplementary Materials B: Gas composition and isotope ratio data from Erebus ice caves and warm
1135 ground

1136 Table B1: Samples analysed by GC-QMS and IRMS, with approximate latitude & longitude

1137 Table B2: Samples analysed by Delta Ray for carbon isotope ratios